Rotational Modulation of the High Frequency Limit of Saturn Kilometric Radiation

Siyuan Wu, Philippe Zarka, Laurent Lamy, Corentin Louis, Shengyi Ye, Renée Prangé, Baptiste Cecconi, William S Kurth

Rotational modulation of the High Frequency Limit of Saturn Kilometric Radiation

Siyuan Wu[1,2], Philippe Zarka[2*], Laurent Lamy[2, 3], Corentin Louis[4], Shengyi Ye[1]*, Renée Prangé[2], Baptiste Cecconi[2], William S. Kurth[5]

[1] Department of Earth and Space Sciences, Southern University of Science and Technology, Shenzhen, Guangdong, People's Republic of China

[2] LESIA, Observatoire de Paris, CNRS, Université PSL, Sorbonne Université, Université Paris Cité, CNRS, Meudon, France

[3] Aix-Marseille Université, CNRS, CNES, LAM, Marseille, France

[4] School of Cosmic Physics, DIAS Dunsink Observatory, Dublin Institute for Advanced Studies, Dublin, Ireland

[5] Department of Physics and Astronomy, University of Iowa, Iowa City, IA, USA

Corresponding author: Philippe Zarka (Philippe.Zarka@obspm.fr) and Shengyi Ye (yesy@sustech.edu.cn)

Key Points:

- The high frequency limit (HFL) of Saturn Kilometric Radiation (SKR) is obtained during the 13-year Cassini mission.
- The average HFL is found to be above and below 600 kHz in the northern and southern hemisphere, respectively.
- A rotational modulation of HFL is verified statistically and by simulation, which excludes a magnetic field anomaly.

Plain Language Summary

Auroral radio emission from Saturn, namely the Saturn Kilometric Radiation (SKR), is generated along high latitude magnetic field lines via the resonance between energetic electrons and a wave's electric field. The first work on the high frequency limit (HFL) of SKR dates back to 1991. Using data from the Voyager Saturn fly-by, scientists found an asymmetry when the HFL is organized by the longitude of the Sun. Based on this asymmetry, a hypothesis about the existence of a magnetic anomaly in Saturn's magnetic field was proposed, which was a novel and breakthrough discovery at that time, but the later Cassini measurements did not confirm this magnetic anomaly. Cassini's expedition around Saturn with 13-year continuous measurements provided an opportunity to re-study the HFL of SKR. The long-term statistics allow us to exclude the magnetic anomaly hypothesis and instead attribute the asymmetry to a modulation which is introduced by an ionospheric/magnetospheric current system at Saturn. A simulation suggests that both temporal and spatial effects play a role to a certain degree. The average frequency and visibility of the HFL are also discussed. These new results provide new insights into the studies of cyclotron maser-related radio emissions.

Abstract

The high frequency limit (HFL) of the Saturnian Kilometric Radiation (SKR) can probe the deepest SKR sources, closest to Saturn's ionosphere. In this study, we determined and analyzed the SKR HFL throughout the entire Cassini Saturn orbital tour. The maximum frequency of the northern SKR, whose distribution peaks at ~ 625 kHz, is shifted by +100 to +200 kHz from the distribution of southern SKR HFL, consistent with the magnetic field offset towards the northern hemisphere at Saturn. The uniformly observed SKR HFL in the vicinity of Saturn suggests a broad extent and beaming of the SKR source. When the observer is confined to certain locations, the rotational modulation of the SKR HFL is clearly observed. This modulation feature of the SKR HFL is statistically established and analyzed in this study. The modulation of HFL is best observed at mid-latitudes between 10° and 40° and at almost all local times. We perform a simulation that suggests that the modulation of HFL requires the superposition of a "clock" like and a rotating source behaviour. By comparing the derived HFL modulation using different longitudes with variable and fixed rotation periods, we can exclude the existence of a magnetic anomaly that was proposed in a previous study based on the Voyager data. The calculation of the least-square periodogram confirms that the modulation observed in HFL is similar to the ones previously detected at Saturn.

1. Introduction

Saturn's Kilometric Radiation (SKR) was discovered in the 1980s during the Voyager 1 Saturn approach (Kaiser et al., 1980) and was later studied in depth by the Cassini mission (Lamy et al., 2008a, 2008b; Cecconi et al., 2009; Fischer et al., 2009, see the review of Lamy, 2017 and refs therein). SKR is generated along auroral magnetic field lines above Saturn's polar regions via the cyclotron maser instability (CMI) (Wu & Lee. 1979; Zarka, 1998; Lamy et al., 2010, 2011, 2018; Mutel et al., 2008; Menietti et al., 2011, Treumann, 2006). It is mainly emitted in the free space Right-Hand Extraordinary (R-X) mode, which is highly circularly polarized with the wave frequency near the local electron cyclotron frequency ($f_{ce}(\,Hz) \sim = 28 * B\ (nT)$ with B the local magnetic field), typically ranging from a few kilohertz (kHz) to 1 megahertz (MHz). Therefore, higher frequency SKR is generated in the region with a stronger magnetic field, i.e., at lower altitudes above the polar regions, if compared to the lower frequency SKR sources. SKR sources were first identified by Voyager to reside on the dawnside sector of the magnetosphere (Kaiser et al. 1982). The later direction-finding analyses of Cassini measurements revealed that SKR sources lie at all longitudes along flux tubes mapping to the main UV auroral oval, while being brighter at dawn (Farrell et al., 2005, Cecconi et al., 2009, Lamy et al., 2009, 2011).

The CMI-produced emissions are beamed at large angles along the surface of a thin (a few degrees wide) hollow cone whose axis is aligned with the local magnetic field in the source (Mutel et al., 2010). This beaming pattern is responsible for a highly anisotropic emission with strong visibility effects, so the observed SKR time-frequency features highly depend on the observers' location (Lamy et al., 2008b, 2013, Cecconi et al., 2009). Because the magnetic field directions in the two hemispheres are opposite, the R-X mode emissions with right-hand polarization with respect to the magnetic field direction would show two different circular polarization senses in the data-derived Stokes parameter related to either north or south. The SKR observed at high latitudes exhibits circular polarization, either >0 (in the south) or <0 (in the north), whereas a superposition of the north and south SKR at the low latitude region produces a very complicated polarization pattern.

SKR activity has been studied and linked to magnetospheric dynamics (Kurth et al., 2005; Jackman et al., 2010; Lamy et al., 2013). The SKR radiated power is strongly correlated with the solar wind dynamic pressure fluctuations (Desch, 1982; Desch & Rucker, 1983; Jackman et al., 2010; Taubenschuss et al., 2006; Zarka et al., 2007). The Low-Frequency Extensions (LFE) of SKR have been used as a proxy for reconnection events and compression-induced hot plasma injections (Bunce et al., 2005; Jackman & Arridge, 2011; Jackman et al., 2009, 2010; Reed et al., 2018). The high frequency limit (HFL) of SKR was also found to be linked mainly to the solar wind dynamics near Saturn, but also to the rotation of the planet (Saturn's longitude) (Galopeau, Ortega-Molina, and Zarka, 1991; Galopeau and Zarka, 1992). While SKR maximal frequencies were measured as high as 1200 kHz using Voyager observations (Kaiser et al., 1980), they remained generally below 1000 kHz when measured from Cassini, with a 50-100 kHz offset of the northern SKR relative to the southern SKR (Lamy et al., 2008a). Long-term variations of the SKR northern and southern maximal frequencies were tested and no relation between the maximal frequency and the solar wind or solar EUV flux was found (Kimura et al., 2013).

The SKR HFL was studied earlier using the data obtained during the Voyager 1&2 Saturn fly-bys. A sinusoidal variation was observed when the HFL was organized as a function of the sub-solar longitude (Galopeau, Ortega-Molina, and Zarka, 1991; Galopeau and Zarka, 1992). This asymmetry was tentatively explained by non-axisymmetric high-order terms in the spherical harmonics decomposition of Saturn's magnetic field, mainly resulting in a magnetic anomaly in Saturn's northern hemisphere. Indeed, for a source fixed in local time (LT) as was thought to be the case for the SKR in the 1990s (Warwick et al., 1981), a rotating magnetic anomaly would cause a periodic variation of f_{ce} in the source while the plasma frequency (f_{pe}) remains constant to first order, leading to a periodic variation of the SKR HFL with the sub-solar longitude (i.e., with the rotation of the planet), as explained in Fig. 4 of Galopeau, Ortega-Molina, and Zarka (1991). During the Cassini era, the subsequent in-situ magnetic field measurements obtained above the northern auroral region did not confirm the presence of such an anomaly (Cao et al., 2011, 2020; Dougherty et al., 2018). The importance of the SKR HFL comes from the fact that it reflects the characteristics of the SKR source regions closest to Saturn, hence probing the high-order terms of the magnetic field and the upper ionosphere. Long-term measurements recorded during the Cassini tour offer the unique possibility to explore further the characteristics of the SKR HFL well beyond the brief Voyager measurements (3-4 months for each fly-by). This work analyzes the SKR HFL obtained from the Cassini radio data during its 13 years in orbit around Saturn. The data and the algorithm developed to find the HFL are described in Section 2. We discuss the observed characteristics of HFL (N/S asymmetry, global distribution, and longitudinal modulation) in Sections 3-6. We compare them to simulations of the SKR visibility in Section 7 and we summarize our results in Section 8.

2. Data and Method

The High Frequency Receiver (HFR) of the Radio and Plasma Wave Science (RPWS) instrument onboard Cassini measured the radio wave electric field from 3.5 kHz to 16.125 MHz (Gurnett et al., 2004). SKR usually covers a broad frequency range, from a few kHz to around one MHz (Kaiser et al., 1980; Lamy et al., 2008a; Kimura et al., 2013). In this work, we analyze the electric field spectrograms over frequencies ranging from 200 kHz to 1300 kHz and from 2004 day 001 (day of year) to 2017 day 258. The wave polarization data (Stokes V, i.e., circular polarization degree, Kraus, 1986) used in this study are obtained from the goniopolarimetric inversion of auto- and cross-correlations of RPWS antenna signals (Cecconi & Zarka, 2005) under the assumptions that either：

(1) The emissions originate from the centre of Saturn; this inversion produces the so-called n3d level data (Cecconi, Lamy, and Zarka, 2017a), or

(2) The emissions are purely circularly polarized, with linear polarization parameters Q=U=0; this inversion produces the n3e level data (Cecconi, Lamy, and Zarka, 2017b). Under this assumption, the

derived circular polarization can also be less than 1 (|V|<1), because of a lower degree of total polarization.

To find the SKR HFL, we first eliminate the unwanted data (e.g., instrumental interference, harmonics of SKR (Wu et al., 2022a)) in the wave intensity and polarization spectrograms. For that purpose, we apply the selection criteria below:

(1) Data points with circular polarization (Stokes V in both n3e and n3d data) value abs(V_{n3e})<0.3 and abs(V_{n3d})<0.3 are deleted from the intensity and circular polarization spectrograms.

(2) Data points with intensity<10 dB are deleted (in n3e and n3d data) from the intensity and circular polarization spectrograms.

Secondly, to mitigate the contamination from low-frequency O mode emissions, e.g., Saturn narrowband emissions (mostly below 70 kHz and mainly near 5 and 20 kHz, Ye et al., 2009; Wu et al., 2021), Saturn Anomalous Myriametric radiation (below 30 kHz, Wu et al., 2022b), and the O mode SKR (below 100 kHz, Lamy et al., 2008a), which are superimposed and mixed with the SKR emissions from time to time, we eliminate the data with frequencies below 200 kHz. Because the O mode SKR emissions are only marginally observed with weaker intensity and the occurrence is relatively rare (Lamy et al., 2008a), the possible high frequency O mode SKR emissions are simply ignored.

A 2-D median filter (with 3*3 channels in the time-frequency plane) is then applied to the processed intensity and circular polarization spectrograms to eliminate isolated emission pixels. Finally, we find the maximum frequency of both the right-hand and left-hand polarized SKR waves at each time step. The data point identified as the maximum frequency should satisfy that: (1) intensity > 20 dB, (2) circular polarization (abs (V)) > 0.3, (3) intensities are continuous below the maximum frequency for at least 4 adjacent frequency channels.

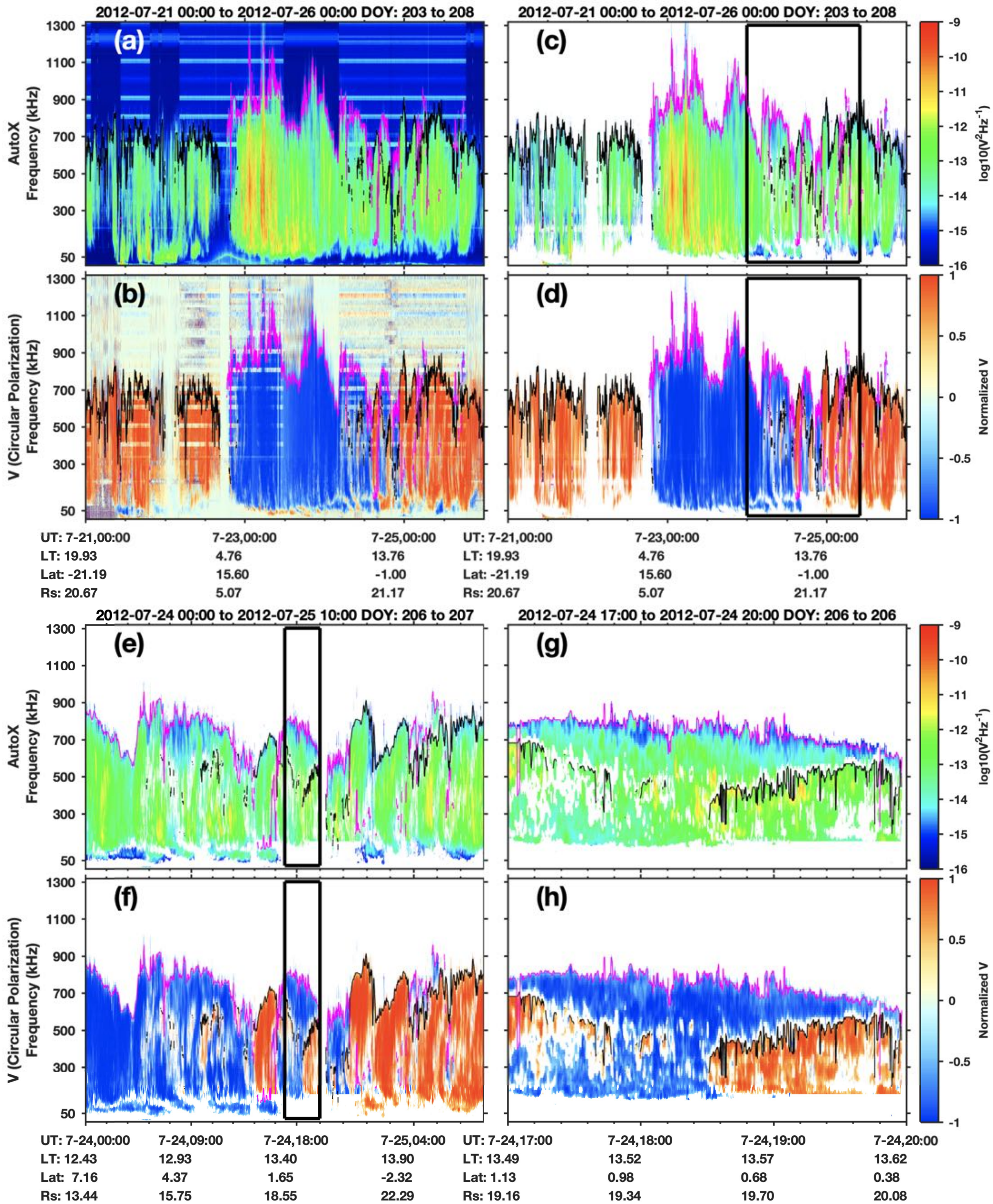

Figure 1. Examples of the identified SKR HFL. Panels (a)-(b) display the RPWS electric field intensity spectrogram and the circular polarization (n3d level data, obtained from the inversion method of Cecconi and Zarka (2005)) over a duration of 5 days. Panels (c)-(d) show the corresponding processed data over

the same interval as Panels (a)-(b). Panels (e)-(f) zoom into the black box of Panels (c)-(d) over a duration of 34 hours. Panels (g)-(h) zoom into the black box of Panels (e)-(f) over a duration of 3 hours. The superimposed pink and black lines mark the identified HFL of the SKR emissions based on the polarization sense, with pink for right-hand and black for left-hand.

The example in Figure 1 illustrates the performance efficiency of the selection criteria in finding the SKR HFL. The unprocessed wave electric field intensity and circular polarization spectrograms from 2012-07-21 to 2012-07-26 are shown in Figure 1 Panels (a)-(b). The processed data and the zoom-in results are given in Panels (c)-(d) and Panels (e)-(h). The overlapped pink and black lines mark the SKR HFL found for the right-hand and left-hand polarized waves, respectively. The obtained HFL lines are well aligned on the top of the SKR emission, suggesting that the algorithm is good enough to capture the temporal variations of the SKR HFL. At low latitudes, the north and south SKR are overlaid together as shown in Figure 1 Panels (f) and (h). The algorithm can pick up both the north and south SKR at each time step according to the polarization sense, e.g., at 07-24 19:00 in Panel (h). Because at low latitudes the lower HFLs from one hemisphere may be polluted by the superposition effect of emissions from the other hemisphere, only the higher HFL is kept at each time step. Finally, 9147518 (~4.64 years) and 6957390 (~3.53 years) HFL values were obtained for the north and south, respectively. The time resolution of the RPWS data is typically 16s and depends on the operation mode of the receiver.

3. The North-South Asymmetry of the SKR HFL

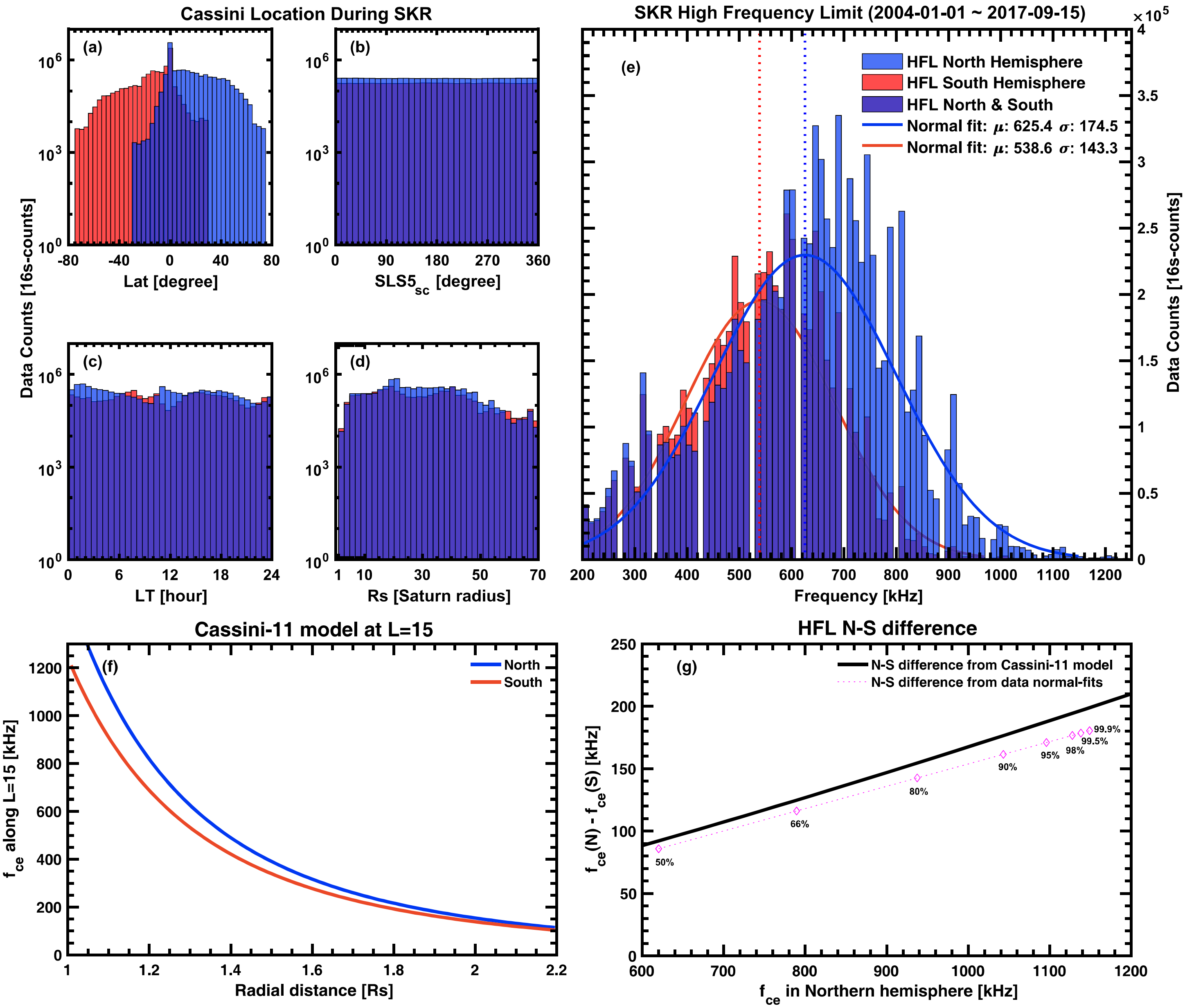

Figure 2. North-South asymmetry of the SKR HFL distributions. Panels (a)-(d): Positions of Cassini during the observation of SKR HFL with (a): Latitude, (b): Longitude of Cassini, derived from the SLS5 system (Ye et al., 2018), (c) Local time, (d) Radial distance. Panel (e): Histogram of the identified SKR HFL with normal fits superimposed. The blue and red bins represent the observations of north and south SKR, respectively. The dark blue color indicates regions with an HFL from both northern and southern SKR (the overlap of light blue and red bars). Panel (f): The f_{ce} values as a function of radial distance calculated using the Cassini-11 magnetic field model (Dougherty et al., 2018) at Lshell=15. The north f_{ce} (blue line) is larger than the south f_{ce} (red line) due to the northward offset of the magnetic field at Saturn. Panel (g): Calculated difference $f_{ce}(r)_{North}$ - $f_{ce}(r)_{South}$ (solid black line) is plotted versus the northern f_{ce}, and compared with that derived from the model fits in Panel (e) (pink dashed line and diamonds). The pink diamonds (frequency differences) are taken at the same percentile from the two curves in Panel (e). The good match confirms that the N-S difference in the HFL is generated by the offset of Saturn's magnetic field.

The average frequency of the north and south SKR HFL are estimated in Figure 2. To check any possible bias caused by the anisotropic beaming pattern of SKR and the observing geometry of Cassini (Lamy et al., 2008a, 2008b, 2013), the positions of Cassini when the SKR HFL are identified are plotted in Figure 2, Panels (a)-(d). The observation positions of Cassini for all Saturn orbits during the 13 year-tour are almost symmetric in the northern and southern hemispheres, which allows us to exclude the uncertainty caused by the geometry effects in estimating the average frequency. The longitude of Cassini used in Panel (b) is derived from the Saturn Longitude System 5 (SLS5, Ye et al., 2018, $\lambda_{sc} = \lambda_{sun}+(12-LT_{sc})*15°$, λ_{sc} is the longitude of the spacecraft, λ_{sun} is the longitude of the sun, LT_{sc} is the spacecraft local time). Because Cassini was inserted in Saturn's orbit from the southern hemisphere in 2004 along orbits with apokrones in the southern hemisphere in the first year of the tour, there is a slight excess of observations of the southern SKR HFL at larger radial distances (not shown), e.g., with radial distance > 70 Rs (Saturn Radius=60268 km). This is a source of bias for the southern HFL at the larger radial distance, and therefore we remove long distance (>70 Rs) observations to eliminate the possible bias in the estimation of the average frequency.

The fitted average SKR HFL frequencies of the north (~625 kHz) and south (~539 kHz) are estimated using normal (Gaussian) fits of the histograms in Figure 2 Panel (e). Note here that the shapes of the histograms in Panel (e) do not fully represent the characteristics of normal distributions, which causes uncertainties for derived average HFL values. However, this rough estimation is sufficient to draw conclusions. The ~87 kHz difference in frequency is consistent with the previous results of a 50-100 kHz range in Lamy et al. (2008a), as previously computed over a more restricted time interval that was proposed to result from the ~0.0466 Rs northward offset of the kronian magnetic field (Lamy et al. 2008a). As SKR is produced close to the local f_{ce} (Lamy et al., 2018), directly proportional to the local magnetic field, the higher average frequency HFL in the north implies that the source region of the northern SKR lies in a position with a stronger magnetic field than the southern SKR source region. The "minimum altitude" of SKR source is primarily determined by the density depletion in the ionosphere and it should be similar in both hemispheres, one can expect similar altitudes of northern and southern SKR sources above the surface of Saturn, because particle densities in the ionosphere rather depend on the gravity field and not on the magnetic field.

Consequently, the explanation of the north-south differences in the average HFL resides in the northward offset of Saturn's magnetic field (the magnetic equator is shifted northward from the planetographic equator by ~0.0466 Rs (Dougherty et al., 2018). Using the Cassini-11 magnetic field model (Dougherty et al., 2018), f_{ce} values along a typical SKR L-shell (L=15, corresponds to invariant latitude = 75°) were calculated and plotted versus the radial distance in both hemispheres in Figure 2 Panel (f). The L-Shell (McIlwain, 1966) corresponds to the distance (normalized to planetary radius) of a dipolar field line apex in the equatorial plane. The calculated f_{ce} in the northern hemisphere is larger than in the southern hemisphere at the same altitudes, and the difference becomes larger at smaller radial distances, which is because the magnetic field decays with the cube of the radial distance. This feature implies that the North-South differences in the HFL will also increase as the HFL increases. A comparison is given in Panel (g), where the calculated difference $f_{ce}(r)_{North}$ - $f_{ce}(r)_{South}$ from the Cassini-11 model is plotted versus the northern f_{ce} (solid black line), and compared with that measured from the normal fits in Panel (e) (pink dashed line with diamonds). The solid black line is directly calculated using the two lines in Panel (f). The pink dashed line with diamonds is calculated using the two normal fits in Panel (e), e.g., the peak-peak frequency difference (difference of 50% - 50% percentile values for the two distributions) is 625.4 kHz – 538.6 kHz ~=87 kHz as indicated by the vertical dashed lines in Panel (e). The percentile values (at 50%, 66%, 80%, 90%, 95%, 98%, 99.5%, 99.9%) of the two normal fits in the two distributions are measured and the corresponding frequency differences are plotted in Panel (g) as the diamonds. The two lines deviate from each other slightly at high frequencies. This is likely due to the fewer data points for HFL at high frequencies and the uncertainty on the normal distribution fits. The good match between the solid black line and the pink dashed line confirms that the magnetic field offset is responsible for the observed difference in the northern and southern SKR HFL.

Another interesting point here is the spread of HFL (sigma values in Figure 2 Panel (e)). The frequency variations in HFL as large as ~400 kHz could be related to solar wind dynamics as suggested by previous studies (Galopeau, Ortega-Molina, and Zarka, 1991; Taubenschuss et al., 2006), similar to the LFE at Saturn (Jackman et al., 2009; Reed et al., 2018). The link between the High- Frequency Extensions (HFE) of SKR and their connection to the solar wind dynamics would be worth a future study.

4. The spatial visibility of the relative SKR HFL

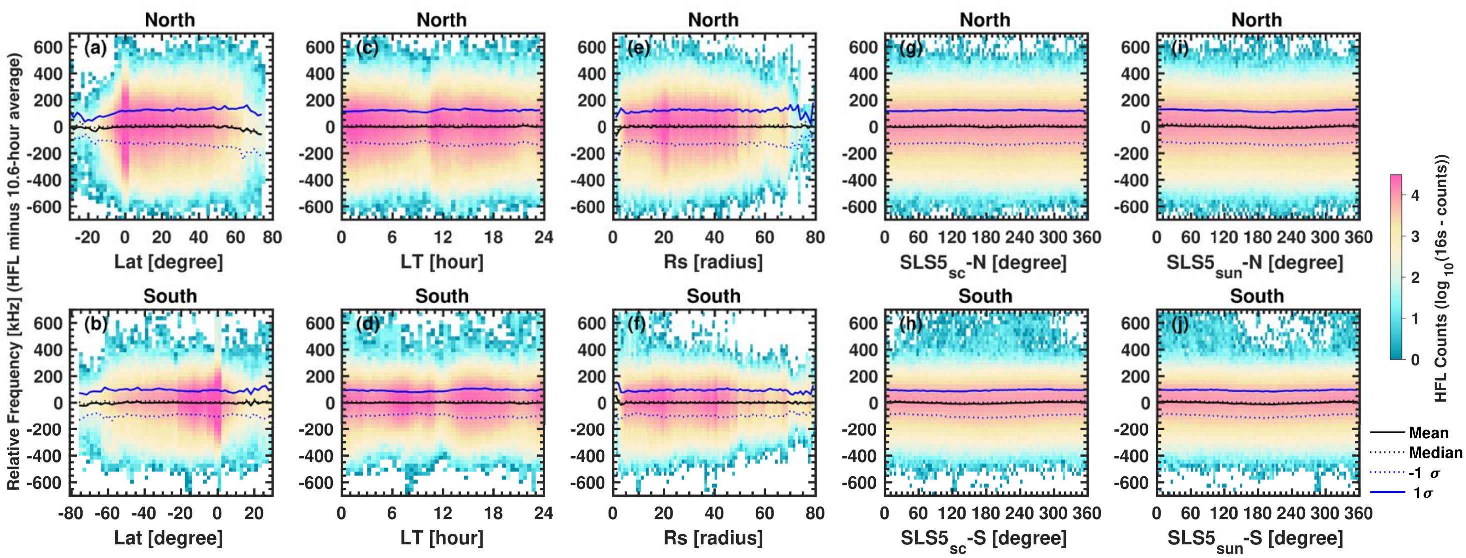

Figure 3. Distributions of the relative HFL. The quantity shown along the y-axis is the relative HFL, i.e., the instantaneous – rotation-averaged HFL. Panels (a)-(b) show the relative HFL distributions in latitude, separately for the northern and southern hemisphere. Panels (c)-(d) and (e)-(f) are the distributions of relative HFL vs local time and radial distance. Panels (g)-(h) and (i) -(j) are the distributions of relative HFL in SLS5 longitude system, using different longitude frames: spacecraft SLS5 in Panels (g)-(h) and sub-solar SLS5 in Panels (i)-(j). The black lines mark the mean (solid) and the median (dashed, nearly superimposed to the mean) relative HFL derived from data with abscissa in the corresponding bin. The blue lines give the +1σ (solid) and -1σ (dashed) extent of the relative HFL distribution at each abscissa.

The distributions of the relative SKR HFL are overplotted in Figure 3 as a function of the location of Cassini (in Latitude, Local Time, Radial distance, and Longitude in Panels (a)-(b), (c)-(d), (e)-(f) and (g)-(h). To eliminate long period, externally-controlled variations of the HFL, e.g., due to the solar wind (Galopeau, Ortega-Molina, and Zarka, 1991; Galopeau and Zarka, 1992), a 10.6 hour (1 Saturn rotation period) running-average was subtracted from the instantaneous HFL. The calculated mean, median and ±1 sigma values of the corresponding relative HFL distributions are overlapped as solid and dashed lines in each panel. Exploring the relative HFL distribution along a single spatial parameter is not rewarding due to the anisotropic beaming of SKR, which couples the different spatial parameters.

All means and medians are flat and close to zero as indicated by the black lines in Figure 3, confirming the absence of bias and suggesting that the beaming of SKR beam statistically covers all spatial regions around Saturn. No particular position is found for which the absolute HFL would be predominantly above or below the 10.6-hour running average. In Panels (a)-(b), more counts are observed at low latitudes (the reddish peak near 0°) because Cassini spent a long time in the equatorial region, but without changing the mean or median. The fewer points of HFL above 60 degrees in latitude in Panels (a)-(b) are because most SKR emissions are observed below 60 degrees. There are also fewer HFL observed beyond a distance of ~50 Saturn radii in Panels (e)-(f), which is due to the fact that Cassini spent most of its time within 50 Saturn radii. There are more points around 20 Saturn radii, because Cassini also spent a long time there, mainly during the numerous Titan fly-bys. Note here that the standard deviations of the relative HFL are always slightly higher in the northern hemisphere than in the southern hemisphere (for all 5 displayed coordinates), which agrees with the general normal fits for north & south HFL in Figure 2 Panel (e). We also organized the relative HFL as a function of sub-solar longitude in Panels (i)-(j) for a first check of a possible asymmetry like the one found in Voyager data (Galopeau, Ortega-Molina, and Zarka, 1991). No such asymmetry is observed. But as 13-year statistics may smooth any asymmetry, we further explore these distributions by restricting the Cassini location to small (LT, latitude) intervals, as discussed in the next Section.

5. The longitudinal modulation of the relative SKR HFL

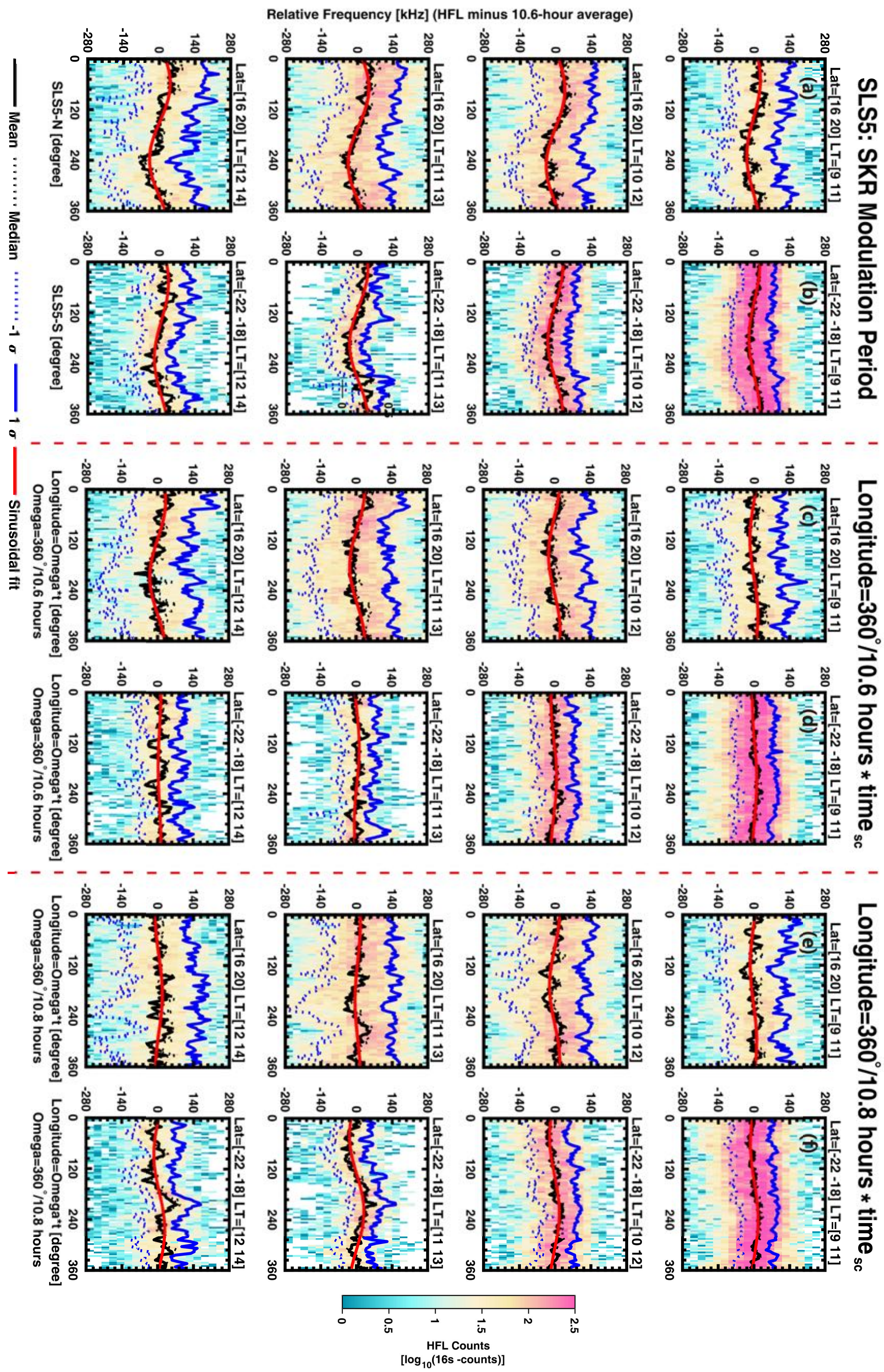
SLS5: SKR Modulation Period
Longitude=360°/10.6 hours * time sc
Longitude=360°/10.8 hours * time sc
Relative Frequency [kHz] (HFL minus 10.6-hour average)
SLS5-N [degree]
SLS5-S [degree]
Longitude=Omega*t [degree] Omega=360°/10.6 hours
Longitude=Omega*t [degree] Omega=360°/10.8 hours
Mean
Median
-1 σ
1 σ
Sinusoidal fit
HFL Counts [log10(16s -counts)]

Figure 4. Examples of longitudinal modulation of the relative SKR HFL. Columns (a)-(b), Examples of the longitudinal modulation of relative SKR HFL observed in the northern and southern hemispheres. Different sub-panels give observations at various (Latitude, LT) positions of Cassini. The black lines show the mean (solid) and median (dashed, hardly visible) relative HFL versus sub-solar longitude (SLS5, Ye et al., 2018). The red lines are the sinusoidal fits of the solid black lines. +1σ and -1σ width of the relative HFL distribution at each abscissa are plotted by solid and dashed blue lines, respectively. Columns (c)-(d) and (e)-(f) repeat the analysis from Columns (a)-(b) but using different longitude systems, derived from different tentative rigid rotation periods of Saturn, 10.6 hours in Columns (c)-(d) and 10.8 hours in Columns (e)-(f).

We restrict the location of Cassini to small spatial bins in local time and latitude (4° Lat × 2 hours LT) to further explore the relative HFL variation as a function of sub-solar longitude. The SLS5 longitude system used in this work is derived from the long-term tracking of average SKR peak intensities. The zero degree of sub-solar longitude in SLS5 corresponds to the maxima of SKR intensity, which usually peaks on the morning side (Ye et al., 2018; Lamy et al., 2009). The SLS5 system follows two time-variable periods, one per hemisphere, clearly distinct (~10.6 h and ~10.8 h) from 2004 until the end of 2008 (Gurnett et al., 2009). The two periods started to converge around the vernal equinox of Saturn in 2009 and crossed each other briefly in late 2009 before starting to oscillate around 10.7 h for four years. The southern period remained at 10.7 h until the end of the mission, whereas the northern period slowed down in 2014 and 2015 to end up at ~10.8 h for the last two years until September 2017 (see the introduction of Ye et al., 2018). The SKR-intensity derived SLS5 naturally contains information on the modulation of SKR generation, which is further related to the modulation of a field-aligned current system at Saturn (Southwood and Cowley, 2014; Provan et al., 2018). When confining the observer to particular LT bins, the sub-solar longitude is related to the spacecraft longitude via a simple shift ($\lambda_{sc} = \lambda_{sun} + (12 - LT_{sc}) \times 15^{\circ}$). The relative HFL observed from a fixed location is then stacked and binned as a function of sub-solar longitude. This procedure allows us to exclude the effects of observation geometry and to mitigate the effect of the SKR beaming.

As shown by the averaged relative HFL (solid black lines) in Figure 4 Columns (a)-(b), the mean relative HFL shows regular quasi-sinusoidal variations as observed from the different locations in local time (different sub-Panels) in both hemispheres. A sinusoidal fit (red lines in Figure 4, $A * sin(\lambda_{sun} + \varphi) + offset$, A: amplitude, φ: phase) is computed for the variations of the average relative HFL in each spatial bin. Broad enough bins in local time (2 hours) and latitude (4 degrees) are needed to gather enough data points in each bin and thus guarantee the accuracy of the calculation of the average relative HFL. In each spatial bin, we require that relative HFL data represent an observation time larger than three Saturn rotation periods (thus ~32 hours). The observation time for each bin is given in Figure A1 in the Appendix. To increase the resolution of the sinusoidal fit, there is a 50% overlap between consecutive bins (i.e., 1 hour steps in LT and 2 degrees in latitude), leading to a total of 816 spatial bins. For the sinusoidal fit in each spatial bin, the root mean square deviation (RMSD) is used to measure the fit quality and discard the poor fits (that correspond to RMSD>0.1; ~40% of the fits have RMSD larger than 0.1; see their distribution in Figure A1).

The sinusoidal variations of relative HFL observed in some bins are reminiscent of the first results from Galopeau, Ortega-Molina, and Zarka, (1991), which was tentatively explained by the presence of a magnetic anomaly. However, in our case the relative HFL is organized as a function of SLS5, which is not related to the rotation of the planet but to that of a particular current system (Ye et al., 2018; Andrews et al., 2011; Cowley and Provan, 2017). To give an intuitive illustration of the SKR intensity and HFL modulation with SLS5, an example is given in Figure A2. The recurring emission occurrence peaks on the spectrum in Figure A2 show the characteristic SKR periodic modulation. The pink lines on top of the SKR emission, as well as the relative HFL in Figure A2 Panel (d), indicate that the HFL & relative HFL also experience a modulation that mirrors the repetition of the SKR emission occurrence peaks.

To explore further whether this modulation in relative HFL could reveal a magnetic anomaly or is controlled by the SLS5 modulation, the relative HFL are further organized by using a series of longitude systems derived assuming fixed rotation periods. For example, in Figure 4 Columns (c)-(d) and (e)-(f) 10.6 hours and 10.8 hours rotation periods are adopted. Should this variation be generated due to a magnetic anomaly that corotates with the planetary magnetic field, the longitude derived using a fixed rotation period should better organize the variation in relative HFL. As can be seen from Figure 4 Columns (c)-(d) and (e)-(f), weaker amplitudes or even lack of modulation are observed when the relative HFL are organized in fixed-period longitude systems. All rotation periods from 10.5 to 11 hours by step of 0.1 hour were also tested (not shown), but none led to a relative HFL longitudinal modulation better organized (i.e. deeper) than the one obtained with SLS5.

For confirmation, a Least-Square-Spectrum-Analysis (LSSA) periodogram was built using the relative HFL series obtained in this study, which is presented in Figure 5. The LSSA, also known as Lomb-Scargle analysis (Lomb, 1976; Scargle, 1982), is a method for estimating the time-frequency spectrum of a time series, which is particularly suitable for the analysis of unevenly sampled data with gaps. The LSSA parameters used to produce Figure 5 are the same as those adopted by Ye et al. (2018). For more information about the LSSA method, readers are referred to Ye et al. (2016, 2018) and Gurnett et al. (2009).

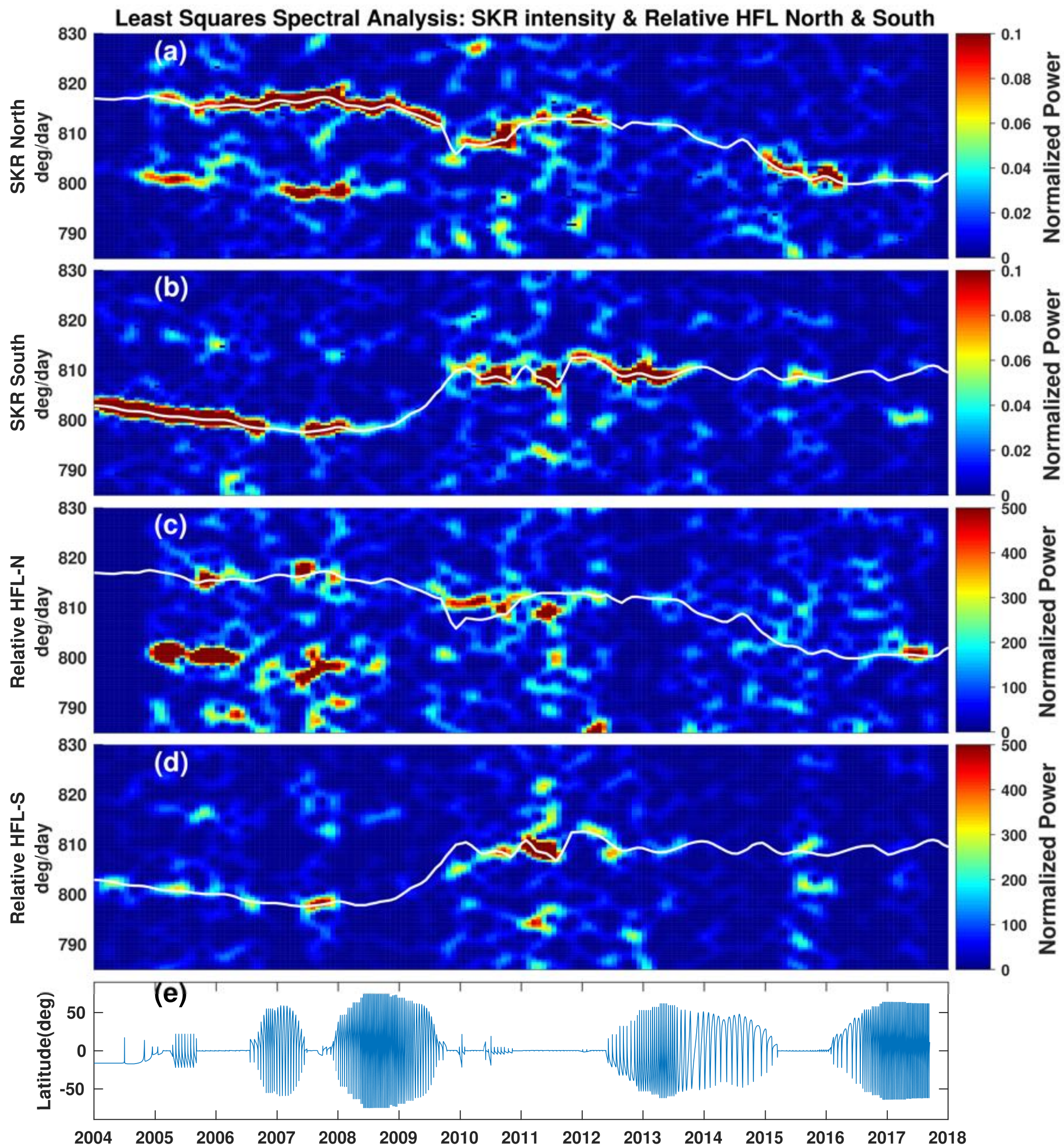

Figure 5. LSSA spectrograms of SKR and relative SKR HFL from 2004 to 2018. The color-coded spectrograms represent the modulation power as a function of universal time on the horizontal axis and modulation rate on the vertical axis. Panels (a)-(d) show the results for the north hemisphere SKR intensity, south hemisphere SKR intensity, north hemisphere relative SKR HFL, and south hemisphere relative SKR HFL, respectively. Panel (e) displays the Cassini latitude during the Saturn orbital tour. The white lines in the four panels represent the northern and southern SKR periods, as derived by Ye et al. (2018). The white lines in Panels (a) and (c) are the same for the north hemisphere SKR, while the white lines in Panels (b) and (d) are the same for the south hemisphere SKR. The relative HFL in Panels (c)-(d) is obtained by subtracting two rotation period average values from the absolute HFL, i.e., instantaneous – 2-rotation-period-averaged HFL.

Panels (a) and (b) of Figure 5 are the SKR intensity modulation spectrograms reproduced from Figure 1 of Ye et al. (2018). The well-known modulation of SKR intensity reveals two distinct periods near 10.6 hours and 10.8 hours for the north and south hemispheres, respectively, and the merging and reversal. The white lines mark the SKR rotational modulation rates for the north in Panel (a) and the south in Panel (b). Panels (c) and (d) show the results of the calculations using the relative HFL time series obtained in this work. The relative HFL series used here are adapted by subtracting the running-mean values of two rotation periods from the absolute HFL values. This was done to mitigate possible bias caused by the process of subtracting one rotation period, as the modulation periods are close to one Saturn rotation period of 10.6 hours. One can easily recognize similar modulation features between the SKR intensity and the relative SKR HFL by comparing Panels (a) and (c), and Panels (b) and (d). Note that the integrated SKR intensities in Panels (a)-(b) are obtained by dividing one rotation period average values from the integrated intensities according to the previous work (Ye et al., 2016; 2018; Gurnett et a., 2009). Therefore, the values of the normalized modulation power in Panels (a)-(b) are smaller, whereas the normalized modulation power in Panels (c)-(d) is larger due to the subtracting process. This calculation directly confirms the modulation of HFL with variable periods and excludes the possibility of constant period modulation or the existence of a magnetic anomaly.

It is interesting to note that the northern SKR (Figure 5 Panels (a) and (c)) also has a second period from early 2005 to the end of 2009 of around 800 deg/day, which is the same period as that of the southern SKR. This might either result from an incorrect separation of northern and southern sources, or electron populations from the south bounce to the north, where they also generate northern SKR with the southern period as suggested by Hunt et al. (2015) and Kivelson and Jia. (2017). It is worth noting that this secondary period of northern SKR at 800 deg/day seems to have a larger modulation signal as the primary northern period around 820 deg/day in the rotational analysis of the relative HFL. Furthermore, there is some deviation in the northern period calculated from the SKR intensity (white line) compared to the result from the relative SKR HFL, and the first deviation can be seen in Panel (c) in the time interval from Saturn equinox (August 2009) until mid-2010. There the relative HFL modulation signal slightly above 810 deg/day is about 3 deg/day higher than the white line. The second deviation occurs during the year 2011, where the rotation of the northern SKR intensity denoted by the white line is about 3 deg/day quicker than the northern HFL modulation signal. This second deviation could be caused by the intense secondary signal from southern hemisphere, but this is not the case for the first deviation. The differences between the SKR modulation period and the one derived from the magnetic field from 2009-2013 were discussed in Fischer et al. (2015), and the relative HFL modulation signal slightly above 810 deg/day from equinox to mid-2010 rather agrees with the period derived from the magnetic field (Cowley and Provan 2016). Other than that, the modulation features between the relative SKR HFL and the SLS5 are quite similar.

6. The distribution and phase of the relative HFL modulation features

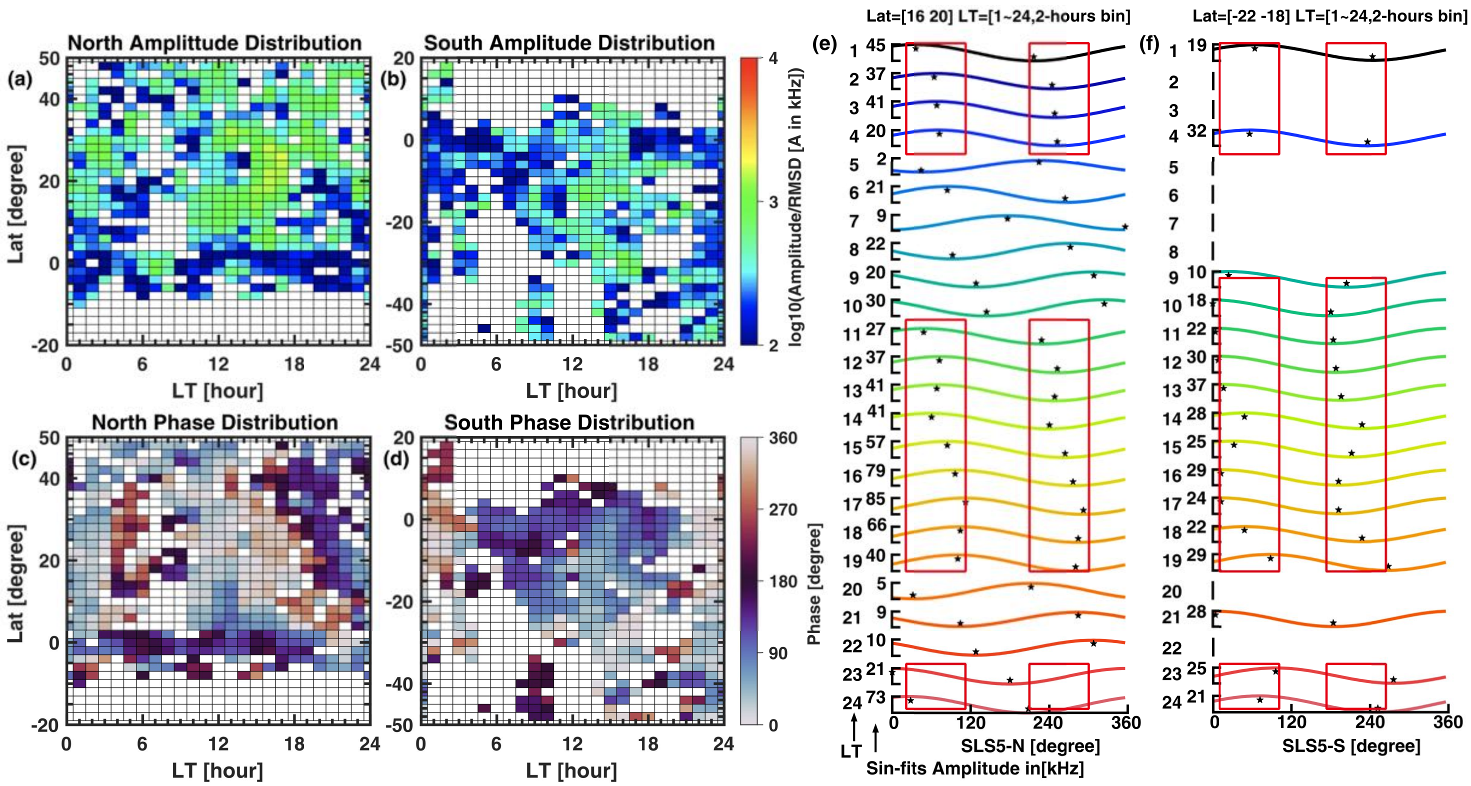

Figure 6. Distribution of the modulation of relative SKR HFL. Panels (a)-(b): distribution of the fitted normalized amplitude of the relative SKR HFL in the north and south as a function of the local time and latitude (amplitude is normalized by the root mean square deviation: A/RMSD, A is the amplitude of the fitted sinusoidal function, RMSD is the calculated root mean square deviation, see more details in Appendix). Panels (c)-(d): same format as the Panels (a)-(b) but for the fitted phase (φ of the sinusoidal function). The bin size of Panels (a)-(d) is [4° Lat $\times$ 2 hours LT] and the RMSD threshold used to discard the poor fits is 0.1. Panel (e): local time slice of the sinusoidal fits of the modulation of the north SKR HFL. The fitted sinusoidal curves in each local time bin are displayed at Lat $= [16^{\circ}\ 20^{\circ}]$ and at Lat $= [-22^{\circ}\ -18^{\circ}]$ for the southern hemisphere in Panel (f). The plotted curves are normalized in amplitude. The real amplitude of each modulation is indicated near the ticks to the left. The red boxes mark the local times where the stronger modulation and relative stable phase of the sinusoidal fits are observed, and the corresponding SLS5 ranges of the maxima (SLS5N=[20° 115°], SLS5S=[5° 110°] for the left-hand side red boxes in both Panels (e) and (f)) and minima (SLS5N=[220° 300°], SLS5S=[170° 260°] for the right-hand side boxes). The black stars for each curve mark the maxima and minima of the sinusoidal functions.

Case studies and statistical direction-finding analyses using Cassini data suggested that SKR sources are distributed at all longitudes along the magnetic field lines mapping to the UV auroral oval, whereas the intensities of SKR maxima are in the morning LT (Cecconi et al., 2009, Lamy et al., 2009, 2011). It has also been known for long that the SKR intensity modulation is best observed in the morning sector (Lamy et al., 2009; Ye et al., 2016; 2018). Therefore, it is interesting to explore further the features of the modulation, i.e., at which place the modulation is stronger? The distribution of the modulation amplitude (with A the amplitude of the fitted sinusoidal function) and phase (φ) of the sinusoidal fit for each spatial bin is then color-plotted as a function of local time and latitude in Figure 6 Panels (a)-(b). The blank bins are due to the lack of data and poor fits. The modulation of relative HFL can be observed in most of the spatial bins as shown by Panels (a)-(b) but with some asymmetries with respect to the latitude and LT.

Strong modulation in both north and south is observed at $abs(Lat) \geq 10^{\circ}$. The modulation amplitude is stronger in the north than in the south. The weaker modulation amplitude observed at $-10^{\circ} \leq Lat \leq 10^{\circ}$ could be due to the beaming geometry of SKR, as the superposition of SKR from the two hemispheres near the equatorial plane may affect the HFL, or may be simply due to the strongly modulated source regions not being visible in these low latitude regions. The phases in Panels (c)-(d)（φ of the sinusoidal functions, $\varphi \sim 0°$ implies that $A * sin(\lambda_{sun} + \varphi)$ function peaks at λ_{sun}~90°）of these regions with strong modulation amplitudes are clustered and show small phases around zero.

In Panel (a) of Figure 6, a region exhibiting weaker modulation and scattered phases can be observed in the morning side LT, e.g., from 5:00 to 10:00 LT. The cause of this phenomenon may be attributed to the shorter observation time in these local times, as suggested in Figure A1 Panels (a)-(b), or it could be due to the merging of signals from numerous intense morning side sources that are continuously distributed throughout the morning sector and continuously illuminate the nearby region at different phases of their modulation. This may result in difficulties for recognizing the modulation features in these bins, as suggested by the large RMSD (poor sinusoidal fits) shown in Figure A1 Panels (b) and (d). Additionally, the modulation also appears weaker from 20:00 to 22:00 LT. Weakly modulated signal from the nearby LT to the 20:00 to 22:00 sector may result in weak modulations seen there.

To give an intuitive illustration of the relative HFL modulation at different LT bins, the fitted sinusoidal curves at Lat = [16°, 20°] in the northern hemisphere are shown in Panel (e) (the 24 sub-panels for different local times are normalized in the vertical direction to address the phase relation, the real (or "physical") amplitude of each curve is indicated near the ticks to the left). The red boxes mark the local time intervals where the stronger modulation and relative stable phase of the sinusoidal fits are consistently observed. The black stars for each curve mark the maxima and minima of the sinusoidal functions. As shown by Figure 6 Panel (e), the curves with larger amplitude mostly show similar modulation phases, e.g., indicated by the red box with LT=11~19 and LT=0~4, whereas the curves with smaller amplitude show dispersed phases, e.g., LT=5~10 and LT=20~23, which could be related to the shorter observation time in the corresponding bins and poor fits caused by the strong modulated morning side SKR sources. The southern modulation pattern has similar features, as shown in Panel (f), for a latitudinal slice at Lat = [-22°, -18°]. The choice of the two latitude slices in Panels (e)-(f) is because these latitudes cover most of the local times as can be seen in Figure 6 Panels (a)-(b), as the other latitudes have more blank bins due to poor fits or lack of data.

7. Simulation of the SKR visibility

To explain the relative HFL modulations observed in Sections 5-6, simple simulations have been carried out using a dipole field with a magnetic moment of 0.21 Gauss and an empirical beaming angle derived from data in a previous work (adopted from the black dashed line in Figure 9 of Lamy et al., 2013). The wave frequencies are assumed to be equal to the local f_{ce}. The SKR sources can be distributed on a set of Lshells of given longitudes, at altitudes corresponding to the emitted frequencies. The SKR spectrogram seen by an observer at a given LT and latitude is obtained by calculating the angles between the location of the observer and the magnetic field vector in SKR sources at each frequency / Lshell / LT / longitude. The frequencies for which these angles match the emission beaming cone are visible for the observer, the others are not. The thickness of the hollow cone wall is set to be 5° in our simulation (Lamy et al., 2013). For one set of given SKR sources, the SKR visibility spectrogram during 1 Saturn rotation is derived by combining the calculations for sources at each time step (corresponding to a specific sub-solar longitude) and noting the highest visible frequency. We set the 0° sub-solar longitude at 12:00 LT to be the first time-step at the start of each calculation.

The relative HFL modulation vs sub-solar longitude observed at certain locations could be generated by either a temporal effect (e.g., a variation in source altitudes generated, e.g., by periodic electron precipitation) or a spatial effect (effects related to the rotation of the planet, e.g., the existence of a complex source structure could produce the HFL variation as the planet is rotating), or both.

To keep the analysis simple, two scenarios were considered: (1) temporal effect: the SKR source is fixed in LT and the source frequencies (altitudes) are changing with time, or equivalently with rotation, as long thought from Voyager results (Warwick et al., 1981). (2) spatial effect: the SKR sources are located at certain longitudes and frequencies (at fixed altitudes, frequencies do not change with time) and the sources corotate with the planet, as evidenced by Cassini measurements (Lamy et al., 2009; Cecconi et al., 2009; Andrews et al., 2011).

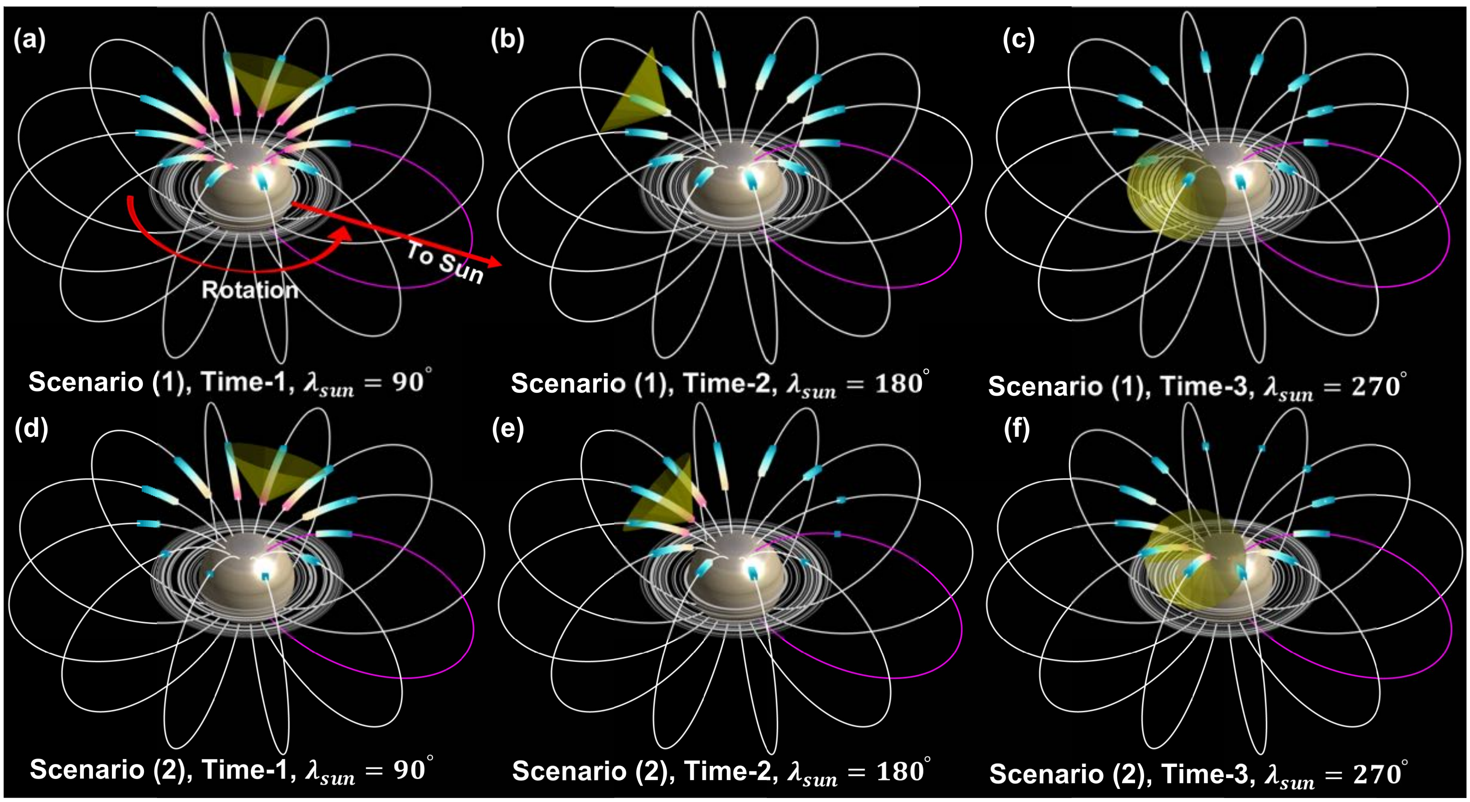

Figure 7. Cartoon illustration of the source configuration for the two Scenarios. Panel (a) displays Saturn with a dipole magnetic field with the SKR sources distributed in the north polar region. The pink magnetic field line is at the sub-solar longitude (LT=12:00, $\lambda_{sun} = 90^{\circ}$). The cyan-red markers show the SKR source configuration in the simulation of Scenario (1). The yellow transparent cone is an example of the SKR beaming. The beaming cone is at $\lambda_{sun} = 90^{\circ}$ in Panel (a) and it rotates to $\lambda_{sun} = 180^{\circ}$ and $\lambda_{sun} = 270^{\circ}$ in Panels (b)-(c). Panels (a)-(c) give the distribution of SKR sources at different simulation time steps. Panels (d)-(f) give the configurations of SKR sources for Scenario (2). Note that the "Time-1" in Panels (a)-(b) with $\lambda_{sun} = 90^{\circ}$ is arbitrarily chosen to mark the time coordinate, which is different from the time-step 1 in the simulation that starts from $\lambda_{sun} = 0^{\circ}$.

In scenario (1), we only assume that the SKR sources are varying sinusoidally in frequency as a function of time because the observed HFL does so. If identical SKR sources are placed at all longitudes and they change together in frequency with a sinusoidal pattern as a function of time, the observer will naturally observe a sinusoidal HFL variation at the same phase at all LT (the observer's latitude being fixed) as illustrated in Figure 7 Panels (a)-(c).

In scenario (2), the complicated source structure could be constructed by simply setting the SKR sources to all longitudes and by giving a different maximum frequency at each longitude, as shown in Figure 7 Panels (d)-(f). As one can imagine, in this case, an observer at a fixed location will thus intersect the hollow cones at different frequencies as the planet rotates, and thus see a changing HFL.

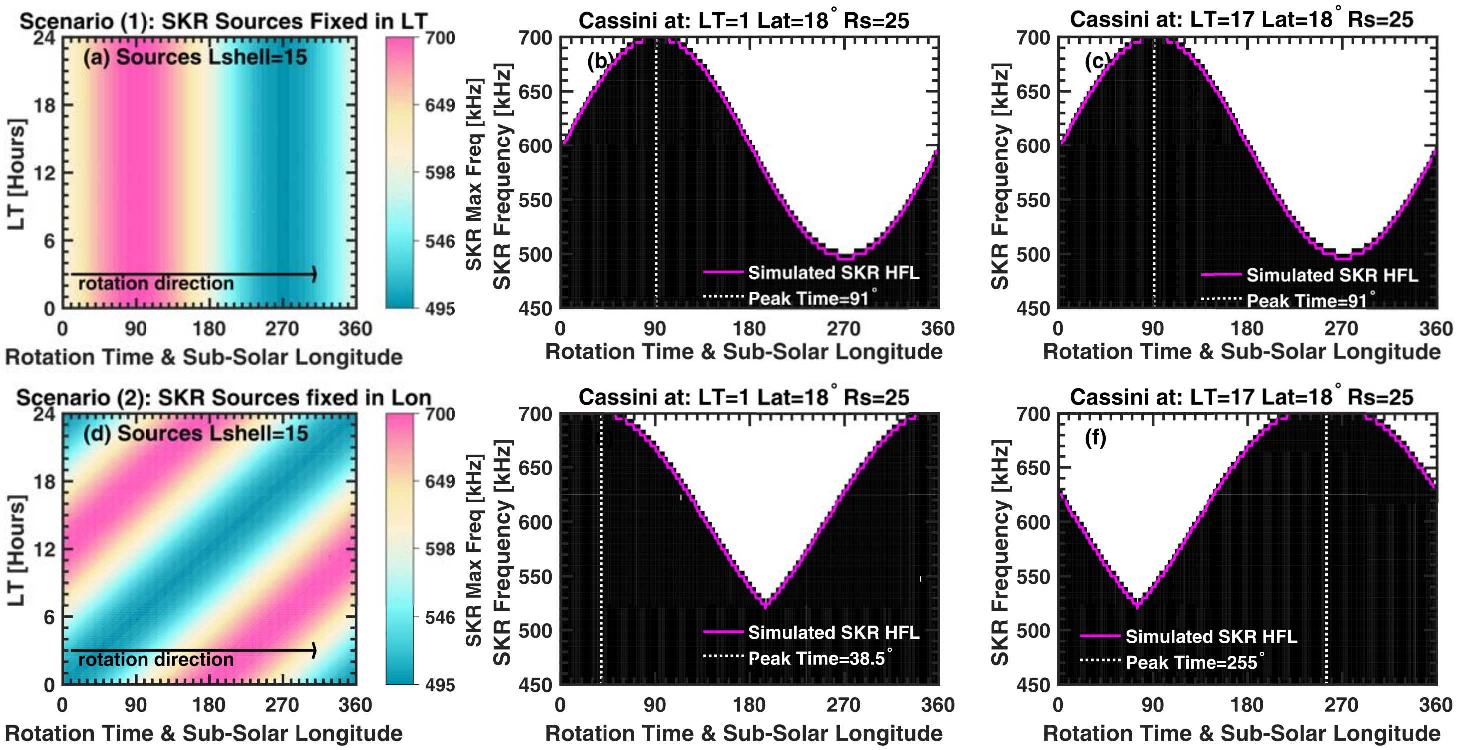

Figure 8. Simulation of the SKR HFL modulations. Panel (a) displays Test 1 for Scenario (1), the SKR sources are fixed in LT range [0:00 -24:00] at Lshell=15. The maximum SKR frequencies are indicated in color code and all the source frequencies are changing together sinusoidally as a function of time / sub-solar longitude. Panels (b)-(c) display the SKR HFL modulations for different observer's locations under the conditions of Scenario (1). Cassini at LT= 01:00, Lat = 18° and Rs=25 Saturn radii in Panel (b) and similar location but at LT=17:00 for Panel (c). Panel (d) displays the source configuration of Scenario (2), the SKR sources are placed at all longitudes. The maximum frequencies of SKR at different longitudes are different and do not change with time. Panels (e)-(f) display SKR visibility spectrograms for different observer's locations (same as Panels (b)-(c)) under the conditions of Scenario (2).

The simulation results are given in Figure 8. For Scenario (1), the LT view of the maximum SKR frequency distribution as a function of time is quantitatively given in Figure 8 Panel (a). All these sources are changing sinusoidally together as a function of time as shown by the color code (only the maximum frequency along each field line is plotted). We arbitrarily distributed the SKR sources between 400 kHz to 700 kHz (step = 5 kHz) at Lshell=15, but taking another range does not change the shape of the results. A sinusoidal variation of the HFL is obtained as indicated by the pink lines in Panels (b)-(c). At any two different local times, i.e., 01:00 for Panel (b) and 17:00 for Panel (c), the HFL peak times are identical and at time step 92, i.e., when the sub-solar longitude reaches 91°.

For Scenario (2), we set the SKR sources along L=15 field lines at all longitudes (1°-360°, step=1°), from 400 kHz to 700 kHz (step = 5 kHz). Then we applied a sinusoidal variation to the frequency range of SKR sources as a function of the longitude as can be seen in Panels (d) in Figure 8. The maximum frequency at each longitude as a function of rotating time is quantitatively given in Figure 8 Panel (d). The color code in Panel (d) suggests that the maximum frequency of a longitude-fixed rotating source produces a complicated pattern in view of a fixed observer at a certain LT and as a function of time. Clear sinusoidal (or quasi-sinusoidal) variations in the HFL are observed in Figure 8 Panels (e)-(f), which is calculated using the source configuration in Figure 8 Panel (d). The observers at different LT observe different phases with the HFL peaking at 38.5° in Panel (e) and 255° in Panel (f), which is similar to the small phase shifts as observed in Figure 6 Panels (e)-(f).

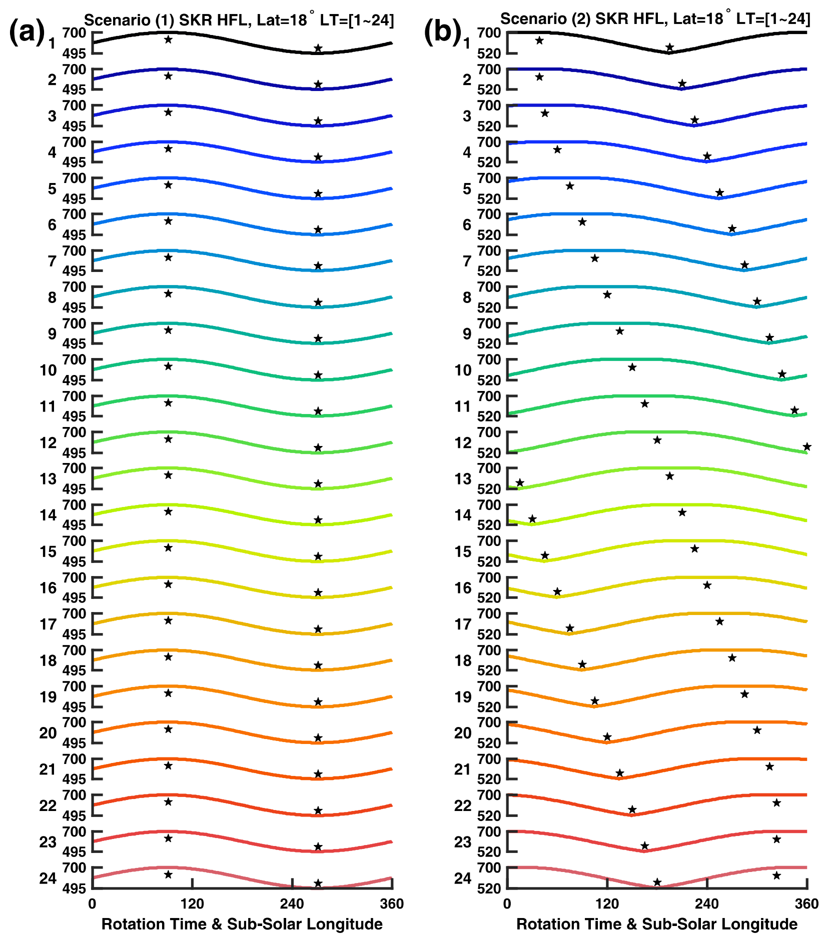

Figure 9. Simulated northern HFL modulation at Lat $= 18^{\circ}$ and different LTs. Format is similar to Figure 6 Panel (e). Panel (a) displays the results of the scenario (1) simulation (LT-fixed but

time-variable sources). Panel (b) displays the results of the scenario (2) simulation (Longitude-fixed, rotating sources).

The simulation results at Lat = 18° and different LTs are given in Figure 9 in the same format as Figure 6 Panels (e)-(f) (at the same latitude with Lat = 18°). The results of Scenario (1) simulation are shown in Figure 9 Panel (a). At all LTs where the SKR is visible, the observed HFL change together with no phase shifts. Results of Scenario (2) simulation displayed in Panel (b) are similar to the results in Panel (a) but with a shift at each LT. These shifts are introduced by the rotation of the planet as shown in Figure 8 Panel (d).

A combination of both scenarios is needed to explain the observations. Scenario (1) provides modulations in HFL with stable phases, and scenario (2) provides intermittent small phase shifts. The maxima and minima of the obtained sinusoidal curves are mostly concentrated at fixed longitudes as indicated by the red boxes in Figure 6 Panels (e)-(f) and only small phase shifts are observed, which are possibly generated by the rotation of the source region as suggested by Scenario (2) simulation. Therefore, the sinusoidal modulation phenomenon of the relative SKR HFL could be generated by the combination of the two simulated situations, that is, the SKR sources corotate with the planet, but many of them show a strong time-variation and may be fixed in local time.

8. Discussion and Summary

The initial understanding of the SKR is a “clock” like source, which means that the SKR sources are fixed in LT and change emission characteristics (intensity, HFL) as a function of time or sub-solar longitude (Warwick et al., 1981; corresponding to Scenario (1) simulation in the last Section), whereas later studies show that the SKR sources also behave as a rotating beam that corotates with the planet and goes over all longitudes with time, along a circumpolar oval whose intensity peaks at dawn (Lamy et al., 2009; Cecconi et al., 2009; Andrews et al., 2011; similar to Scenario (2) simulations). Hence the modulation of SKR tends to be a combination of the temporal and spatial effects, as shown by Cassini radio direction-finding and magnetic measurements (Lamy, 2011, Andrews et al., 2011) and modeled in our Scenarios. The same is found for the relative HFL modulation studied in this work.

The source altitudes of the SKR rely on both the CMI conditions (i.e., f_{pe}/f_{ce}) and the electron distribution (Wu & Lee, 1979; Lamy et al., 2009, 2018). The CMI condition is not likely to cause the source altitude variation because the plasma density at the SKR source region is mainly related to the ionospheric plasma density, which decays exponentially. The ~ 1 rotation period modulation of relative HFL can be observed both on the dayside and on the nightside, which suggests the ionospheric conductance does not play a major role in producing the modulation. Hence the formation of the shell-like electron distribution is a likely reason for the modulation of the source altitudes, which is further related to particle transport and associated current systems. The corotating source structure could be formed naturally because electron precipitation is different at different longitudes, leading to the formation of complex source regions. Further details to understand the SKR source variations would require simulations of the electron precipitation, forming of the field-aligned currents and calculation of the wave growth rate, which are beyond the scope of this work.

The previous work of Galopeau, Ortega-Molina, and Zarka, (1991) analyzed Voyager-Saturn data for 3-4 months around each fly-by to study the SKR HFL. Because the fly-bys of the Voyager spacecraft only covered limited local time and latitude ranges, these authors also observed a sinusoidal variation of the relative HFL as a function of sub-solar longitude. Their explanation of this variation in terms of a magnetic field anomaly was a logical one (that can be reproduced by our simulations). More than 40 years after the Voyager Saturn fly-bys in 1980 & 1981, having Cassini observations at all LT and latitudes, having discovered the SLS5 system with variable N & S periods, having checked that no single rigid rotation period can explain the observed relative HFL modulations better than SLS5, and having the direct calculation of the HFL modulation spectrograms, we can conclude that this modulation is related to the SKR current systems and refute the need for a magnetic anomaly.

This present work makes it possible to obtain all the SKR HFL during the 13 years of Cassini's orbital tour around Saturn by using an automatic detection algorithm. The characteristics of HFL are analyzed. The average HFL in the northern hemisphere is at 625 kHz, and at 539 kHz in the south. The difference in the average frequency between the two hemispheres is produced by the northward offset of the Saturnian magnetic field. The SKR HFL can cover almost all the regions in the vicinity of Saturn as seen in the quite uniform distribution of HFL. Sinusoidal modulation of the relative SKR HFL is observed when the data are restricted to small spatial bins and organized as a function of sub-solar longitude. The LSSA calculation using the relative HFL time series directly confirms the modulation of relative HFL at the SLS5 modulation periods and hence excludes the possibility of the existence of a magnetic anomaly. Simulation results suggest that the modulation could be explained by a rotating SKR source superimposed with a strong temporal modulation, which is consistent with the previous studies. The source structure and the variation could be related to the electron precipitation processes in the SKR source regions, and this may be covered in a future study.

Appendix

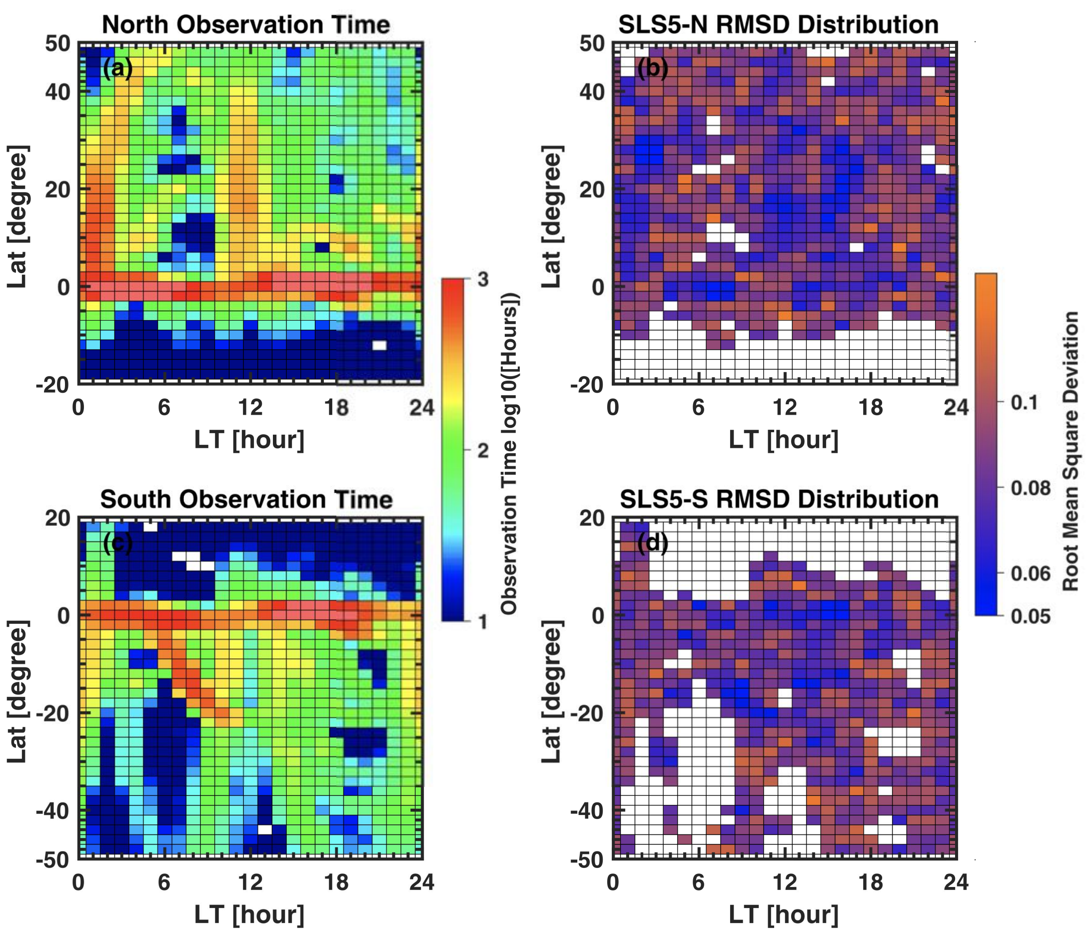

Figure A1. Observation time and the RMSD in each of the spatial bins. Panel (a) gives the observation time of Cassini in each spatial bin when the north HFL is observed. Panel (b) give the calculated RMSD for the sinusoidal fits of the relative HFL with respect to the SLS5 longitude when using SLS5-N. Panels (c)-(d) give the results in the same format as Panels (a)-(b) but for the southern hemisphere.

The observation time and the calculated RMSD of the sinusoidal fits are given in Figure A1. The calculated results of the spatial bins shown in Figure 6 Panels (a)-(b) have to satisfy two criteria: (1) data inside each bin must have an observation time larger than 3 rotation periods (1 Saturn rotation time ≅ 10.6 hours); (2) The RMSD value is less than 0.1 (roughly 40% of all the bins exhibit RMSD >0.1).

RMSD defined as: $\sqrt{\frac{1}{n}\sum_{i=1}^{n}(\mathrm{A} * \sin(longitude(i) + \varphi) - mean_{hfl}(longitude(i)))^2}$, n is the number of the data points in the fitting. Here n=90 since we use a longitude step = 4°. A and φ are the amplitude and phase obtained by the fittings, respectively. As can be seen from the comparison between the calculated RMSD in Figure A1 Panels (b) and (d) and the modulation amplitude in Figure 6 Panels (a)-(b), the fitted bins with smaller RMSD also show a stronger modulation amplitude in general. The poorly-fitted bins with larger RMSD usually show rather random patterns, so that their removal does not affect the results.

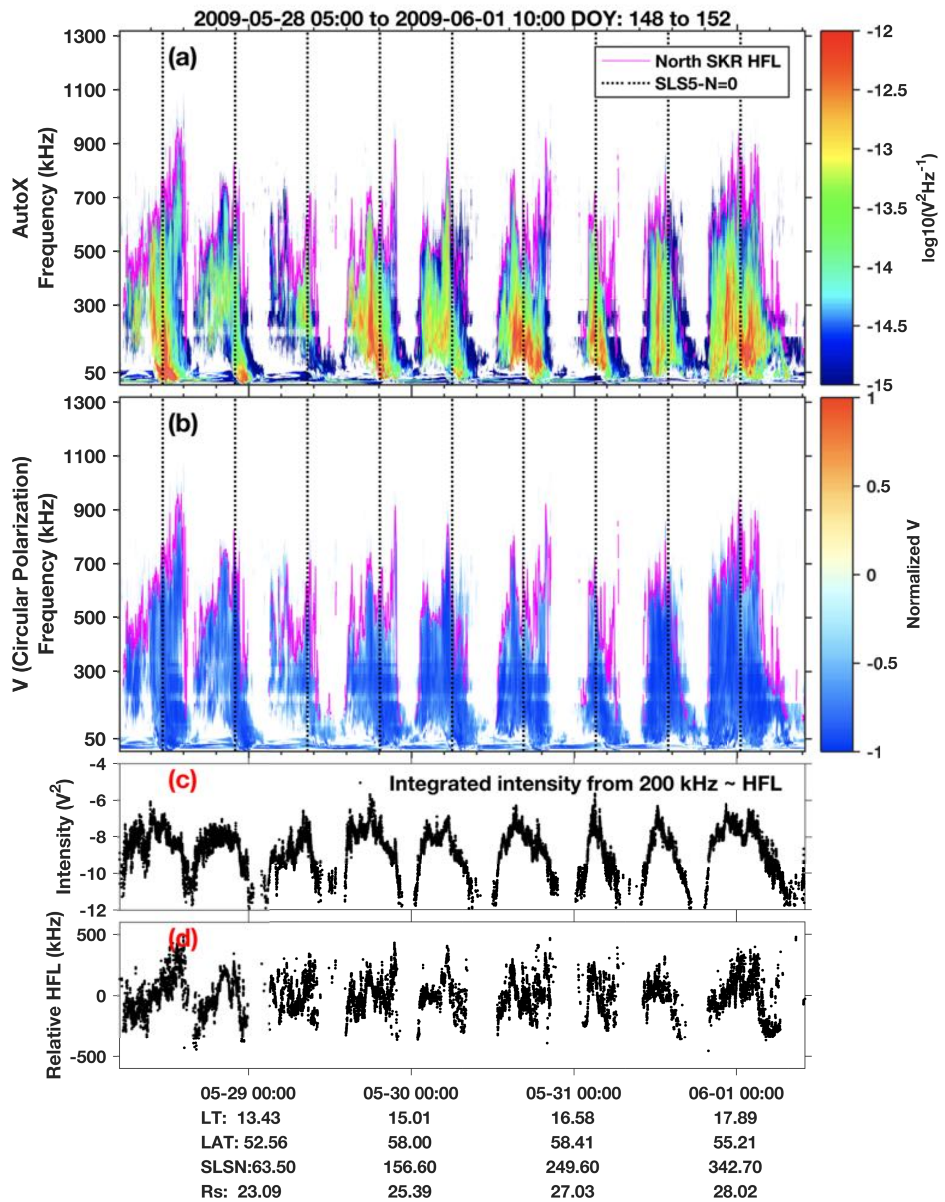

Figure A2. Modulation of SKR intensity and HFL. Panel (a) presents the RPWS electric field intensity spectrogram, processed using the same methodology as Panels (c)-(d) in Figure 1. Panel (b) displays the circular polarization (n3d level data). The overlapping pink line represents the identified SKR HFL. The black dotted lines indicate the instances when SLS5-N reaches zero. Panel (c) gives the integrated SKR intensity (integrated from 200 kHz to HFL) using the data in Panel (a). Panel (d) gives the relative HFL values derived from the pink lines above and by subtracting out the 10.6 hours running average values.

Figure A2 demonstrates the modulated occurrence of SKR as seen by a distant observer. A linear frequency axis (y-axis) is used to emphasize the HFL variations. The origin of the SKR emissions in Figure A2 is in the northern hemisphere, as indicated by the negative polarization values in Panel (b) and the associated latitudes below. The black dotted lines indicate the points where SLS5-N reaches 0 degree, which closely align with consecutive peaks in SKR intensity. The pink lines on top of the SKR emission, as well as the SKR intensity (in Panel (c)) and relative HFL (in Panel (d)), indicate that the HFL & relative HFL also experience a modulation that mirrors the repetition of the SKR emission peaks.

Acknowledgments

This work was supported by the Strategic Priority Research Program of the Chinese Academy of Sciences (grant No. XDB 41000000). SYW is also supported by China Scholarship Council. PZ, LL and BC acknowledge support from the PNP and PNST programs from CNRS/INSU, and from the CNES. CKL's work at the Dublin Institute for Advanced Studies was funded by the Science Foundation Ireland Grant 18/FRL/6199. SYW thanks for the helpful discussion of Mingzhe Liu and Zhongying Lu on this work.

Open Research

The Cassini RPWS data used in this work were downloaded from the LESIA/Kronos collection of n2 level (Cecconi, Lamy, and Zarka, 2017c), n3d level (Cecconi, Lamy, and Zarka, 2017a), n3e level (Cecconi, Lamy, and Zarka, 2017b) (goniopolarimetric inversion results obtained following the method of Cecconi & Zarka. 2005). The derived SKR HFL data is also available from MASER service via a doi link: (https://doi.org/10.25935/dz99-s514).

References

Andrews, D. J., Cecconi, B., Cowley, S. W. H., Dougherty, M. K., Lamy, L., Provan, G., & Zarka, P. (2011). Planetary period oscillations in Saturn's magnetosphere: Evidence in magnetic field phase data for rotational modulation of Saturn kilometric radiation emissions. Journal of Geophysical Research: Space Physics, 116(A9). https://doi.org/https://doi.org/10.1029/2011JA016636

Bunce, E. J., Cowley, S. W. H., Wright, D. M., Coates, A. J., Dougherty, M. K., Krupp, N., et al. (2005). In situ observations of a solar wind compression-induced hot plasma injection in Saturn's tail. Geophysical Research Letters, 32(20). https://doi.org/https://doi.org/10.1029/2005GL022888

Cao, H., Dougherty, M. K., Hunt, G. J., Provan, G., Cowley, S. W. H., Bunce, E. J., et al. (2020). The landscape of Saturn's internal magnetic field from the Cassini Grand Finale. Icarus, 344, 113541. https://doi.org/https://doi.org/10.1016/j.icarus.2019.113541

Cao, H., Russell, C. T., Christensen, U. R., Dougherty, M. K., & Burton, M. E. (2011). Saturn's very axisymmetric magnetic field: No detectable secular variation or tilt. Earth and Planetary Science Letters, 304(1), 22–28. https://doi.org/https://doi.org/10.1016/j.epsl.2011.02.035

Cecconi, B., Lamy, L., Zarka, P., Prangé, R., Kurth, W. S., & Louarn, P. (2009). Goniopolarimetric study of the revolution 29 perikrone using the Cassini Radio and Plasma Wave Science instrument high-frequency radio receiver. Journal of Geophysical Research: Space Physics, 114(A3). https://doi.org/https://doi.org/10.1029/2008JA013830

Cecconi, B., & Zarka, P. (2005). Direction finding and antenna calibration through analytical inversion of radio measurements performed using a system of two or three electric dipole antennas on a three-axis stabilized spacecraft. Radio Science, 40(3), 1–20. https://doi.org/10.1029/2004RS003070

Cecconi, B., Lamy, L., & Zarka, P. (2017a). Cassini/RPWS/HFR LESIA/Kronos N3d Data Collection (Version 1.0) [Data set]. PADC. https://doi.org/10.25935/5JFX-DH49

Cecconi, B., Lamy, L., & Zarka, P. (2017b). Cassini/RPWS/HFR LESIA/Kronos N3e Data Collection (Version 1.0) [Data set]. PADC. https://doi.org/10.25935/9ZAB-FP47

Cecconi, B., Lamy, L., & Zarka, P. (2017c). Cassini/RPWS/HFR LESIA/Kronos N2 Data Collection (Version 1.0) [Data set]. PADC. https://doi.org/10.25935/XS9J-ND90

Cowley, S. W. H. & Provan, G. Planetary period modulations of Saturn's magnetotail current sheet during northern spring: Observations and modeling. J. Geophys. Res. Sp. Phys. 122, 6049–6077 (2017).

Cowley, S. W. H., & Provan, G. (2016). Planetary period oscillations in Saturn's magnetosphere: Further comments on the relationship between post-equinox properties deduced from magnetic field and Saturn kilometric radiation measurements. Icarus, 272, 258–276. https://doi.org/https://doi.org/10.1016/j.icarus.2016.02.051

Desch, M. D., & Rucker, H. O. (1983). The relationship between Saturn kilometric radiation and the solar wind. Journal of Geophysical Research: Space Physics, 88(A11), 8999–9006. https://doi.org/https://doi.org/10.1029/JA088iA11p08999

Desch, M. D. (1982). Evidence for solar wind control of saturn radio emission. Journal of Geophysical Research: Space Physics, 87(A6), 4549–4554. https://doi.org/https://doi.org/10.1029/JA087iA06p04549

Dougherty, M. K., Cao, H., Khurana, K. K., Hunt, G. J., Provan, G., Kellock, S., et al. (2018). Saturn's magnetic field revealed by the Cassini Grand Finale. Science, 362(6410), eaat5434. https://doi.org/10.1126/science.aat5434

Farrell, W. M., Desch, M. D., Kaiser, M. L., Lecacheux, A., Kurth, W. S., Gurnett, D. A., et al. (2005). A nightside source of Saturn's kilometric radiation: Evidence for an inner magnetosphere energy driver. Geophysical Research Letters, 32(18). https://doi.org/https://doi.org/10.1029/2005GL023449

Fischer, G., Cecconi, B., Lamy, L., Ye, S.-Y., Taubenschuss, U., Macher, W., et al. (2009). Elliptical polarization of Saturn Kilometric Radiation observed from high latitudes. Journal of Geophysical Research: Space Physics, 114(A8). https://doi.org/https://doi.org/10.1029/2009JA014176

Fischer, G., Gurnett, D. A., Kurth, W. S., Ye, S.-Y., & Groene, J. B. (2015). Saturn kilometric radiation periodicity after equinox. Icarus, 254, 72–91. https://doi.org/https://doi.org/10.1016/j.icarus.2015.03.014

Galopeau, P., Ortega-Molina, A., & Zarka, P. (1991). Evidence of Saturn's magnetic field anomaly from Saturnian kilometric radiation high-frequency limit. Journal of Geophysical Research, 96(A8), 14129–14140. https://doi.org/10.1029/91JA00696

Galopeau, P., & Zarka, P. (1992). Reply [to "Comment on 'Evidence of Saturn's magnetic field anomaly from saturnian kilometric radiation high-frequency limit'"]. Journal of Geophysical Research: Space Physics, 97(A8), 12291–12297. https://doi.org/https://doi.org/10.1029/92JA00323

Gurnett, D. A., Kurth, W. S., Kirchner, D. L., Hospodarsky, G. B., Averkamp, T. F., Zarka, P., et al. (2004). The Cassini Radio and Plasma Wave Investigation. Space Science Reviews, 114(1), 395–463. https://doi.org/10.1007/s11214-004-1434-0

Gurnett, D. A., Persoon, A. M., Groene, J. B., Kopf, A. J., Hospodarsky, G. B., & Kurth, W. S. (2009). A north-south difference in the rotation rate of auroral hiss at Saturn: Comparison to Saturn's kilometric radio emission. Geophysical Research Letters, 36(21). https://doi.org/https://doi.org/10.1029/2009GL040774

Hunt, G. J., Cowley, S. W. H., Provan, G., Bunce, E. J., Alexeev, I. I., Belenkaya, E. S., et al. (2015). Field-aligned currents in Saturn's northern nightside magnetosphere: Evidence for interhemispheric current flow associated with planetary period oscillations. Journal of Geophysical Research: Space Physics, 120(9), 7552–7584. https://doi.org/https://doi.org/10.1002/2015JA021454

Jackman, C. M., & Arridge, C. S. (2011). Statistical properties of the magnetic field in the Kronian magnetotail lobes and current sheet. Journal of Geophysical Research: Space Physics, 116(A5). https://doi.org/https://doi.org/10.1029/2010JA015973

Jackman, C. M., Arridge, C. S., Slavin, J. A., Milan, S. E., Lamy, L., Dougherty, M. K., & Coates, A. J. (2010). In situ observations of the effect of a solar wind compression on Saturn's magnetotail. Journal of Geophysical Research: Space Physics, 115(A10). https://doi.org/https://doi.org/10.1029/2010JA015312

Jackman, C. M., Lamy, L., Freeman, M. P., Zarka, P., Cecconi, B., Kurth, W. S., et al. (2009). On the character and distribution of lower-frequency radio emissions at Saturn and their relationship to substorm-like events. Journal of Geophysical Research: Space Physics, 114(A8). https://doi.org/https://doi.org/10.1029/2008JA013997

Kaiser, M. L., Desch, M. D., Warwick, J. W., & Pearce, J. B. (1980). Voyager detection of nonthermal radio emission from Saturn. Science, 209(4462), 1238–1240.

Kaiser, M. L., & Desch, M. D. (1982). Saturnian kilometric radiation: Source locations. Journal of Geophysical Research: Space Physics, 87(A6), 4555–4559. https://doi.org/https://doi.org/10.1029/JA087iA06p04555

Kivelson, M. G., & Jia, X. (2018). Coupled SKR Emissions in Saturn's Northern and Southern Ionospheres. Geophysical Research Letters, 45(7), 2893–2900. https://doi.org/https://doi.org/10.1002/2017GL075425

Kimura, T., Lamy, L., Tao, C., Badman, S. V, Kasahara, S., Cecconi, B., et al. (2013). Long-term modulations of Saturn's auroral radio emissions by the solar wind and seasonal variations controlled by the solar ultraviolet flux. Journal of Geophysical Research: Space Physics, 118(11), 7019–7035. https://doi.org/https://doi.org/10.1002/2013JA018833

Kurth, W. S., Gurnett, D. A., Clarke, J. T., Zarka, P., Desch, M. D., Kaiser, M. L., et al. (2005). An Earth-like correspondence between Saturn's auroral features and radio emission. Nature, 433(7027), 722–725. https://doi.org/10.1038/nature03334

Kraus, J. D. (1966). Radio astronomy (pp. 116–125). McGraw-Hill.

Lamy, L. (2017). The Saturnian kilometric radiation before the Cassini Grand Finale. In G. Fischer, G. Mann, M. Panchenko, & P. Zarka (Eds.), Planetary Radio Emissions VIII (pp. 171–190). https://doi.org/10.1553/PRE8s171

Lamy, L., Cecconi, B., Prangé, R., Zarka, P., Nichols, J. D., & Clarke, J. T. (2009). An auroral oval at the footprint of Saturn's kilometric radio sources, colocated with the UV aurorae. Journal of Geophysical Research: Space Physics, 114(A10). https://doi.org/https://doi.org/10.1029/2009JA014401

Lamy, L., Prangé, R., Pryor, W., Gustin, J., Badman, S. V, Melin, H., et al. (2013). Multispectral simultaneous diagnosis of Saturn's aurorae throughout a planetary rotation. Journal of Geophysical Research: Space Physics, 118(8), 4817–4843. https://doi.org/https://doi.org/10.1002/jgra.50404

Lamy, L., Zarka, P., Cecconi, B., Prangé, R., Kurth, W. S., & Gurnett, D. A. (2008a). Saturn kilometric radiation: Average and statistical properties. Journal of Geophysical Research: Space Physics, 113(A7). https://doi.org/https://doi.org/10.1029/2007JA012900

Lamy, L., Zarka, P., Cecconi, B., Hess, S., & Prangé, R. (2008b). Modeling of Saturn kilometric radiation arcs and equatorial shadow zone. Journal of Geophysical Research: Space Physics, 113(A10). https://doi.org/https://doi.org/10.1029/2008JA013464

Lamy, L., Zarka, P., Cecconi, B., Prangé, R., Kurth, W. S., Hospodarsky, G., et al. (2018). The low-frequency source of Saturn's kilometric radiation. Science, 362(6410), eaat2027. https://doi.org/10.1126/science.aat2027

Lamy, L., Cecconi, B., Zarka, P., Canu, P., Schippers, P., Kurth, W. S., et al. (2011). Emission and propagation of Saturn kilometric radiation: Magnetoionic modes, beaming pattern, and polarization state. Journal of Geophysical Research: Space Physics, 116(4), 1–16. https://doi.org/10.1029/2010JA016195

Lamy, L., Schippers, P., Zarka, P., Cecconi, B., Arridge, C. S., Dougherty, M. K., et al. (2010). Properties of Saturn kilometric radiation measured within its source region. Geophysical Research Letters, 37(12), 1–6. https://doi.org/10.1029/2010GL043415

McIlwain, C. E. (1966). Magnetic coordinates. Space Science Reviews, 5(5), 585–598. https://doi.org/10.1007/BF00167327

Menietti, J. D., Mutel, R. L., Schippers, P., Ye, S.-Y., Gurnett, D. A., & Lamy, L. (2011). Analysis of Saturn kilometric radiation near a source center. Journal of Geophysical Research: Space Physics, 116(A12). https://doi.org/https://doi.org/10.1029/2011JA017056

Mutel, R. L., Christopher, I. W., & Pickett, J. S. (2008). Cluster multi-spacecraft determination of AKR angular beaming. Geophysical Research Letters, 35(7), L07104. https://doi.org/https://doi.org/10.1029/2008GL033377

Mutel, R. L., Menietti, J. D., Gurnett, D. A., Kurth, W., Schippers, P., Lynch, C., et al. (2010). CMI growth rates for Saturnian kilometric radiation. Geophysical Research Letters, 37(19). https://doi.org/https://doi.org/10.1029/2010GL044940

Provan, G. et al. Planetary Period Oscillations in Saturn's Magnetosphere: Cassini Magnetic Field Observations Over the Northern Summer Solstice Interval. J. Geophys. Res. Sp. Phys. 123, 3859–3899 (2018).

Reed, J. J., Jackman, C. M., Lamy, L., Kurth, W. S., & Whiter, D. K. (2018). Low-Frequency Extensions of the Saturn Kilometric Radiation as a Proxy for Magnetospheric Dynamics. Journal of Geophysical Research: Space Physics, 123(1), 443–463. https://doi.org/10.1002/2017JA024499

Southwood, D. J. & Cowley, S. W. H. The origin of Saturn's magnetic periodicities: Northern and southern current systems. J. Geophys. Res. Sp. Phys. 119, 1563–1571 (2014). doi: 10.1002/2013JA019632

Taubenschuss, U., Rucker, H. O., Kurth, W. S., Cecconi, B., Zarka, P., Dougherty, M. K., & Steinberg, J. T. (2006). Linear prediction studies for the solar wind and Saturn kilometric radiation. Annales Geophysicae, 24(11), 3139–3150. https://doi.org/10.5194/angeo-24-3139-2006

Treumann, R. A. (2006). The electron–cyclotron maser for astrophysical application. The Astronomy and Astrophysics Review, 13(4), 229–315. https://doi.org/10.1007/s00159-006-0001-y

Warwick, J. W., Pearce, J. B., Evans, D. R., Carr, T. D., Schauble, J. J., Alexander, J. K., et al. (1981). Planetary Radio Astronomy Observations from Voyager 1 Near Saturn. Science, 212(4491), 239–243. https://doi.org/10.1126/science.212.4491.239

Wu, C. S., & Lee, L. C. (1979). A theory of the terrestrial kilometric radiation. The Astrophysical Journal, 230(July), 621. https://doi.org/10.1086/157120

Wu, S.Y., Ye, S.Y., Fischer, G., Wang, J., Long, M., Menietti, J. D., et al. (2021). Statistical Study on Spatial Distribution and Polarization of Saturn Narrowband Emissions. The Astrophysical Journal, 918(2), 64. https://doi.org/10.3847/1538-4357/ac0af1

Wu, S.Y., Zarka, P., Lamy, L., Taubenschuss, U., Cecconi, B., Ye, S.Y., et al. (2022a). Observations of the First Harmonic of Saturn Kilometric Radiation During Cassini's Grand Finale. Journal of Geophysical Research: Space Physics, 127(9), e2022JA030776. https://doi.org/https://doi.org/10.1029/2022JA030776

Wu, S. Y., Ye, S. Y., Fischer, G., Taubenschuss, U., Jackman, C. M., O'Dwyer, E., et al. (2022b). Saturn Anomalous Myriametric Radiation, a New Type of Saturn Radio Emission Revealed by Cassini. Geophysical Research Letters, 49(16), e2022GL099237. https://doi.org/https://doi.org/10.1029/2022GL099237

Ye, S.-Y., Fischer, G., Kurth, W. S., Menietti, J. D., & Gurnett, D. A. (2018). An SLS5 Longitude System Based on the Rotational Modulation of Saturn Radio Emissions. Geophysical Research Letters, 45(15), 7297–7305. https://doi.org/https://doi.org/10.1029/2018GL077976

Ye, S.-Y., Gurnett, D. A., Fischer, G., Cecconi, B., Menietti, J. D., Kurth, W. S., et al. (2009). Source locations of narrowband radio emissions detected at Saturn. Journal of Geophysical Research: Space Physics, 114(A6). https://doi.org/https://doi.org/10.1029/2008JA013855

Ye, S.-Y., Fischer, G., Kurth, W. S., Menietti, J. D., & Gurnett, D. A. (2016). Rotational modulation of Saturn's radio emissions after equinox. Journal of Geophysical Research: Space Physics, 121(12), 11,711-714,728. https://doi.org/https://doi.org/10.1002/2016JA023281

Zarka, P. (1998). Auroral radio emissions at the outer planets: Observations and theories. Journal of Geophysical Research: Planets, 103(E9), 20159–20194. https://doi.org/https://doi.org/10.1029/98JE01323

Zarka, P., Lamy, L., Cecconi, B., Prangé, R., & Rucker, H. O. (2007). Modulation of Saturn's radio clock by solar wind speed. Nature, 450(7167), 265–267. https://doi.org/10.1038/nature06237